Franz-Josef Schmitt et al.. (2013) *Signpost Open Access J. NanoPhotoBioSciences*. **1**, 1-45.
Volume 01, Article ID 010301, 45 pages

REVIEW ARTICLE **Open Access**

Signpost Open Access Journal of NanoPhotoBioSciences

Journal Website: http://signpostejournals.com

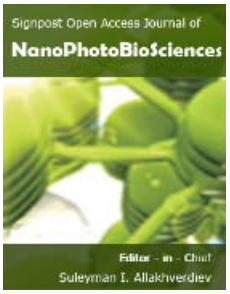

Structural Organization and Dynamic Processes in Protein Complexes Determined by Multiparameter Imaging

Franz-Josef Schmitt[a,*], Evgeny Maksimov[b], Cornelia Junghans[a], Jörn Weißenborn[a], Patrick Hätti[a], Vladimir Z. Paschenko[b], Suleyman I. Allakhverdiev[c,d], Thomas Friedrich[a]

[a]Institute of Chemistry, Biophysical Chemistry, TU Berlin, Straße des 17. Juni 135, D-10623 Berlin, Germany; [b]Department of Biophysics, Biology Faculty, Lomonosov Moscow State University, 119991 Moscow, Russia; [c]Controlled Photobiosynthesis Laboratory, Institute of Plant Physiology, Russian Academy of Sciences, Botanicheskaya Street 35, Moscow 127276, Russia; [d]Institute of Basic Biological Problems, Russian Academy of Sciences, Institutskaya Street 2, Pushchino, Moscow Region 142290, Russia

*Corresponding author: E-mail: schmitt@physik.tu-berlin.de

Received: April 18, 2013

Accepted: May 2, 2013

Abstract

A combination of complementary spectroscopic techniques was used to determine certain structural parameters and excitation energy transfer (EET) processes in biological pigment-protein complexes and fluorescent proteins. While a single spectroscopic technique does not provide unambiguous data related to the structural organization, and since only dynamic processes in a restricted temporal domain can be gathered, we present examples in which the combination of complementary techniques is suitable to deliver a complete picture of a certain parameter set. First, EET processes in light harvesting complexes of the cyanobacterium A. marina were determined. Structural details of the macroscopic organization are visualized by transmission electron microscopy (TEM) while the migration of excited states is analyzed with time resolved ps-fluorescence spectroscopy and compared with published results from fs-pump-probe spectroscopy. Second, the theory of Förster Resonance Energy Transfer (FRET) was used to correlate the distance between transition dipole

moments with dynamical processes that are accessible with highly time-resolved studies. With FRET, the average distance between semiconductor nanocrystals attached to photosynthetic light harvesting complexes was determined. Furthermore, the configuration of a strongly excitonically coupled Chl dimer in the water soluble Chl binding protein WSCP of class IIa from cauliflower genetically expressed in E. coli and reconstituted with Chl a, Chl b or mixtures of Chl a and Chl b was analyzed. Details on the pigment-protein interaction between Chl and the protein backbone in WSCP represent structural details that are accessible by the thorough theoretical analysis of ultrafast exciton relaxation processes, time-resolved fluorescence spectroscopic and site-selective hole-burning studies. Third, the combination of time-resolved and time-integrated fluorescence spectroscopy with fluorescence correlation spectroscopy (FCS) allowed the estimation of the distance between dipole moments of donor and acceptor in FRET pairs containing enhanced green fluorescent protein (eGFP) as donor and red fluorescent (tagRFP) protein as acceptor. Simultaneously, the hydrodynamic radius of the eGFP-tagRFP-FRET construct was determined. This hydrodynamic radius is by a factor of four bigger than the dipole distance determied by FRET, and also about four times as big as the size of the construct from available crystal structures. Therefore, internal degrees of freedom seem to hamper the diffusion of the flexible FRET construct, which cannot be decribed as a homogeneous sphere as done by the simplified calculation of the hydrodynamic radius from diffusion.

The given examples summarize typical strategies of a combined analysis of multiple parameters by complementary techniques that allow the determination of the structural organization of complex biological macromolecules and the dynamics of bioenergetic processes in such structures such as excitation energy transfer.

1. Introduction

The photophysical and biochemical properties of chlorophyll molecules in photosynthetic complexes are tuned by coupling of the pigments to neighbouring pigment molecules or binding to specific protein environments. This principle has developed in the biosphere by evolution and led to amazing structures with highest efficiency in light harvesting, transfer of electronically excited states and transformation of light into electrochemical free energy (Mimuro, 2004; Schmitt, 2011).

Up to date, it has not been possible to transfer this principle to a technical application in order to construct a nanoscaled machine of comparable complexity and stability like the photosynthetic apparatus in higher plants or photosynthetic bacteria. The full understanding of the relevance and function of molecular interaction processes in photosynthetic pigment-protein complexes (PPC) might be helpful in many application fields. Therefore, the determination of structural and dynamical parameters in living matter is a crucial scientific challenge.

Applications for artificially designed PPC are e.g. nanoscaled intelligent organic antenna systems for photovoltaics, which could act as innovative light-harvesting complexes raising and/or regulating the absorption cross section of photovoltaic cells (Lebedev et al., 2006; Schmitt et al., 2012). Other applications are intelligently switchable PPC that undergo state transitions from an inactive to an active state when illuminated or when in contact to certain environments. Such PPC could e.g. be applicable in the photodynamic therapy of skin cancer and reduce the toxicity of the applied photodynamic dyes (Yoon et al., 2013).

Nanobiophotonics is a common description for the investigation of nanoscaled processes in living matter with light. The more general expression of nanophotobiosciences summarizes not only spectroscopic and microscopic methods, where light is used as the instrument of investigation, but expands the scientific approach to all techniques and samples that are biological, nanoscopic and involve the interaction of light and (living) matter.

In the first part of this review, we summarize studies on photosynthetic organisms presented in form of exemplary findings regarding our nanophotonic

research performed on photosynthetic light harvesting antenna complexes, mainly the phycobiliprotein (PBP) antenna of cyanobacteria (Petrášek et al., 2005; Schmitt et al., 2006; Theiss, 2006; Schlodder et al., 2007; Theiss et al., 2008; Lambrev et al., 2011; Schmitt, 2011), specific pigment-protein complexes with unknown function like the water soluble chlorophyll binding protein (WSCP) (Renger et al., 2007, 2009; 2011; Theiss et al., 2007; Schmitt et al., 2008; Pieper et al., 2011) and hybrid complexes containing inorganic nanocrystals and photosynthetic light harvesting complexes (Schmitt, 2010; Schmitt et al., 2011, 2012). Such studies can be extended to whole organisms (Petrášek et al., 2005; Schmitt et al., 2006), and higher plants (Belyaeva et al., 2008, 2011).

In detail, the power of complementary techniques to determine excitation energy transfer processes as well as the pigment-pigment coupling are the focus of this review. Mostly indirect methods like fs-absorption spectroscopy (Theiss, 2006; Renger et al., 2007; Theiss et al., 2007, 2008) or time-resolved difference absorption techniques (Schlodder et al., 2007), site-selective spectroscopic studies like fluorescence line narrowing and hole burning studies (Pieper et al., 2011), fluorescence spectroscopy and especially Förster Resonance Energy Transfer studies (FRET) (Petrášek et al., 2005; Schmitt et al., 2006, 2008, 2011, 2012; Schmitt, 2010, 2011; Lambrev et al., 2011) as well as theoretical analyses (Renger et al., 2007, 2009, 2011) provide deep insight into the configuration of coupled pigments, the interaction with the environment (Barinov et al., 2009) and the excited state dynamics in these structures. The studies on photosynthetic samples as presented in chapter 3 are already published in different single publications and the PhD thesis of Schmitt (2011) as mentioned at the corresponding positions in this manuscript.

A strong improvement of results gained from single spectroscopic or microscopic studies of complex hierarchically structured samples is achieved by a study of the decomposed sample (Schmitt, 2011). However, the experimental results might depend on the sample preparation and the measurement setup. It is therefore necessary to compare various results for consistency and to investigate the influence of the sample preparation and experimental manipulation on the experimental results. In the case of the investigation of PBP and WSCP, combined results of time- and wavelength-correlated single photon counting, time- and wavelength-resolved fs-absorption changes, ground state absorption spectroscopy, hole burning spectroscopy, transmission electron microscopy and theoretical analysis, sometimes based on additional experiments (e.g. CD spectroscopy (Renger et al., 2007, 2009)) were used to complete the picture. Other complexes (LHC aggregates) were additionally studied with atomic force microscopy (AFM) (Lambrev et al., 2011).
It might be useful to accomplish a kind of methodical statistics of the experimental techniques (Schmitt, 2011). In this case, the scientist can shift systematic aberrations to statistical uncertainties to a certain extent. For this purpose, the researcher has additionally to be able to reproduce the sample frequently enough without variation.

In most cases, the principal resolution is not limited by the setup but by the heterogeneity of the sample or even the uncertainty of the observed states. By performing high-resolution fluorescence nanoscopy (Hell, 2004; Westphal et al., 2005; Westphal, Hell, 2005) or advanced atomic force microscopy (Gross et al., 2009), we shift the source of uncertainty from the optical wavelength characteristically used in our measurement setup to the observed states, which is an ultimate resolution limit.

Due to the huge impact of fluorescence proteins in nanobiophotonics, recent studies performed on genetically expressed proteins which are derived from the green fluorescent protein (GFP) (Tsien, 2008) are presented as the second part of this review.

The discovery of FPs and their application in fluorescence microscopy provided new insights into the complicated and fascinating world of life on the microscopic scale. This application in highly resolved fluorescence nanoscopy was boosted by the development of photoswitchable derivatives of GFP (Andresen et al., 2005, 2007; Hofmann et al., 2005; Dedecker et al., 2007; Eggeling et al., 2007; Brakemann et al., 2011). As FPs are specific markers

that can be fused as tags to selected proteins, it became possible to follow the dynamics of a certain protein or enzyme in the living cell with minimal disturbance of the cell and its metabolism.

The synergistic interplay between highly resolved fluorescence microscopy (Hell, 2004; Westphal et al., 2005; Westphal, Hell, 2005) and photoswitchable fluorescence proteins lead to a brilliant new methodology that broke the diffraction barrier of optical microscopy and abolished dogmas of the achievable resolution. Next to the diffusion of proteins, also the protein-protein interaction can be observed by Förster-Resonance-Energy-Transfer on the basis of single interacting molecules. Sophisticated techniques like the study of the conformational dynamics of ion channels and ion transporters became feasible by the combination of fluorescence spectroscopy and voltage-clamp techniques (voltage-clamp fluorimetry) (Geibel et al., 2003; Dempski et al., 2009).

Therefore, it seems most promising to choose FPs for a thorough study of nanostructures. In comparison to solid state physics, which is well described in terms of a quantum mechanical formalism, probability fluctuations and thermodynamic processes play an important role in biophysics. Still, an accurate description of protein dynamics has yet to be developed. The progress of solid state physics is partially based on the possibility to approximate the solid state by a periodic grating that can be treated quantum mechanically. This approach cannot be simply transformed to biophysics of macromolecules. Erwin Schrödinger called the living system a nonperiodic solid state (Schrödinger, 1989).

Being mostly derivatives or relatives of GFP, FPs are genetically encoded and thus enable genetic engineering in order to achieve or develop certain photophysical or photochemical properties. This can even be done by directed evolution combining mutation and selection processes to achieve certain desired special properties of such proteins (Brakemann et al., 2011).

FRET processes are very prominent examples showing that complementary techniques are very helpful to determine pigment-pigment coupling. However, analyses based on the fluorescence amplitudes of donor and acceptor alone can give rise to misleading conclusions, if spectral crosstalk is not compensated for, or if the donor is quenched by the presence of the acceptor without an efficient energy transfer to the acceptor (Schmitt et al., 2012), or if donor and acceptor chromophores are not expressed in a fixed 1:1 stoichiometric ratio.

In addition, the pure time-resolved analysis of FRET processes might contain dangerous artefacts, if the EET occurs on a long time scale (e.g. in the order of the fluorescence decay time of the acceptor itself), or if the acceptor gains energy from molecules different from the investigated donor.

We present studies performed on FRET constructs comprising GFP and tagRFP as parts of a single fusion protein. The combined analysis of FRET evaluating fluorescence amplitudes and time-resolved fluorescence and fluorescence correlation spectroscopy (FCS) delivered insights into the nanoscaled distance of the transition dipole moments in GFP (donor) and tagRFP (acceptor) and the hydrodynamic radius of the FRET construct.

After the investigation of all systems mentioned above, it could be shown that fluorescence spectroscopy represents a tool for the study of ps-processes even with pulses, which are 100 ps in full width of half maximum, if and only if the system and the sample are sufficiently stable and the investigated sample consists of a sufficiently small number of coupled states (e.g. max. two coupled two level systems). In that case the resolution is rising with the squareroot of the energy used for the measurement, similar to the results of highly spatially resolved fluorescence nanoscopy (Hell, 2004; Westphal et al., 2005; Westphal, Hell, 2005). The principal limitations allow a much better resolution than widely assumed (Schmitt, 2008, 2009).

In marked contrast to this optimistic interpretation, it was shown that a unique analysis of ultrafast single energy transfer steps is not possible, if a system is too complex (more complex than the mentioned two coupled excited states). In the latter case, it is

intrinsically impossible to extract information on the accurate values of the single energy transfer steps, if the dynamics of the different coupled states takes place in the same time domain (e.g. all steps occur on the 10-ps time scale, i.e. within 10-100 ps) (Belyaeva et al., 2008; Schmitt, 2011). An improvement can only be achieved by a study of the single components of the sample or by the employment of complementary experimental techniques up to a kind of methodical statistics of the experimental techniques. To a certain extent the experimenter can shift systematic aberrations to statistical uncertainties employing different experimental techniques.

The field of highly resolved structural and dynamic analysis has undergone a boost in the last decades. The main reasons are i) the progress in sample preparation (e.g. crystal preparation of photosynthetic complexes for x-ray diffraction (Yano et al., 2006)), ii) the development and improvement of many different experimental techniques like nonlinear polarisation spectroscopy in the frequency domain (NLPF) (Krikunova et al., 2002), photon-echo spectroscopy (Agarwal et al., 2000), hole burning spectroscopy (Pieper et al., 2000), total internal reflection fluorescence microscopy (TIRF), fluorescence lifetime imaging nanoscopy (FLIN) and many more, and iii) the strong progresses in high resolution fluorescence microscopy, which broke the diffraction barrier in the far field regime (Hell, 2004; Andresen et al., 2005, 2007; Hofmann et al., 2005; Westphal et al., 2005; Westphal, Hell, 2005; Dedecker et al., 2007; Eggeling et al., 2007; Brakemann et al., 2011). From the latter techniques, especially stimulated emission depletion microscopy (STED) and photo-activation localization microscopy (PALM) should be mentioned. The physical understanding of these techniques starting from the bottom of the most basic physical principles is still in progress and an absolute barrier for the resolution of structure arrangement and temporal dynamics with optical techniques in the visual regime is still not clearly formulated and a matter of debate (Talaga, 2006; Schmitt, 2008, 2009).

Therefore, this work does not only present new results in highly resolved ps-fluorescence spectroscopy but should also help to understand their limitations. Especially the combination of different techniques, a field which is still under development, is of high interest and promises success which might help to shift nanobiophotonics to picobiophotonics and femtobiophotonics not only on the time domain but also regarding the spatial resolution. Promising complementary and partially compatible techniques are e.g. atomic force microscopy (AFM) and fluorescence spectroscopy especially to investigate energy transfer processes between the AFM tip and the investigated sample (Vickery, Dunn, 2000; Sarkar et al., 2004).

The ultimate goal would be to extract all information from a system which is *a priori* experimentally accessible. If a sample is endowed with long-term stability or can be reproduced often enough, it is important to make long time observations (Vitali, 2011) and to combine more than one experimental technique to extract the available information as completely as possible, because every technique has a maximum of accessible information content and typical technical problems result in systematic aberrations of the results. By combining several experimental techniques, the experimenter transfers the systematic deviations to statistical ones. Statistic deviations can be improved just by averaging more results. In the future, we will focus on the possibilities to extract this information, which is not fully resolved yet.

2. Materials and methods

The complementary methods used which are presented in the following sections comprise the applied fluorescence techniques. Additional absorption spectroscopic methods, site selective spectroscopy, theoretical considerations and further techniques mentioned are well described in the cited literature. The fluorescence techniques covering the presented studies are time- and wavelength resolved fluorescence spectroscopy based on the single photon counting technique (TWCSPC) (section 2.1), photoluminescence emission spectroscopy (PLE) and time-integrated fluorescence spectroscopy (section 2.2) and fluorescence lifetime imaging microscopy (FLIM) performed with a newly developed

multiparameter setup combining wide field microscopy, confocal laser scanning microscopy and fluorescence correlation spectroscopy (FCS) (section 2.3). The FLIM setup is equipped with new detection systems for time-resolved fluorescence microscopy as a high throughput quadrant anode (QA) microchannel plate detector and three single photon avalanche diodes for autocorrelation and two-channel cross-correlation (see section 2.3).

2.1. Time- and wavelength-resolved fluorescence spectroscopy

For studies on light emission in the short time regime (10 ps – 100 ns) a TCSPC setup with spectral resolution was constructed as shown in Figure 1. The system combines the advantages of the high optical throughput of a multi anode detector system with 16 output (anode) elements (PML-16 C, Becker&Hickl, Germany (Becker & Hickl GmbH, 2006a, 2006b)) allowing the registration of up to 10^6 counts/sec. with the sensitive technique of SPC and the big advantages of a mobile setup. The fibre-based optics allows the targeted spectroscopy of samples in glass cuvettes, on surfaces or of whole leaves of higher plants, for details see (Schmitt, 2011). Various pulsed lasers or LEDs can easily be connected as excitation light sources.

Figure 1 shows the TWCSPC setup with optical path in blue for excitation from the laser source via optional polarizer and short pass filter (SP). The sample temperature can be varied with a Peltier cooling device or a cryostatic system as described in the text and in ref. (Schmitt, 2011). The fluorescence light (red) is monitored via analyzer (optional), grey filters and long pass (LP) filter. The spectrometer system is connected with the multianode photomultiplier PML 16-C. The PMT signal is processed via constant fraction discriminator (CFD), time-to-amplitude converter (TAC) and analog-to-digital converter (ADC).

The PML 16-C is combined with a 120 mm crossed Czerny-Turner polychromator (MultiSpec, LOT) equipped with a 600 grooves/mm grating as a dispersive element, the space coordinate along the delay line correlates with the wavelength (Becker & Hickl GmbH, 2006b). Using the polychromator with a 600 grooves/mm grating, the spectral bandwidth of the PML-16 C is 12.5 nm / channel. Dependent on the wavelength, the emitted photons are deflected onto the

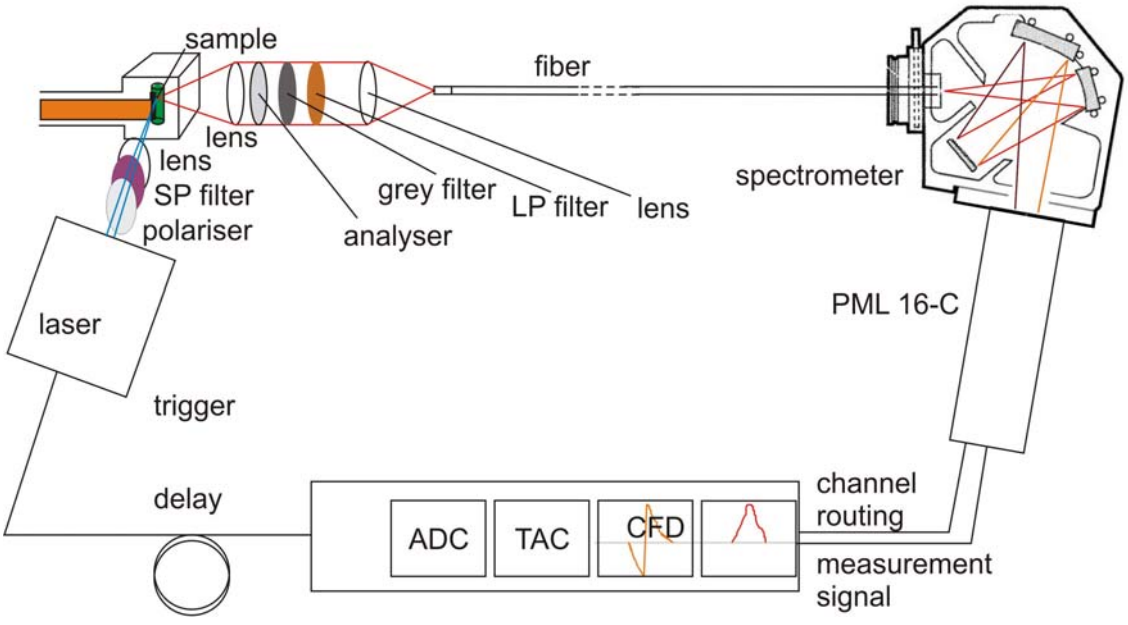

Figure 1. Measurement setup used for TWCSPC. For details, see text and ref. (Schmitt, 2011). The figure was published in (Schmitt, 2011).

corresponding channel in a grating mash used in the PML 16-C that guides the electron avalanche to the corresponding anode element (Becker & Hickl GmbH, 2006b). The output signal of the PML 16-C is further processed by the SPC-530 card (Becker&Hickl, Germany) containing CFDs and TACs. The data is stored in a digital multichannel analyser and processed by a personal computer. Each of the 16 wavelength channels contains 4096 channels in the time domain corresponding to temporal resolution (time coordinate of the fluorescence decay). The wavelength coordinate is determined by the position of the polychromator grating (Becker & Hickl GmbH, 2006a, 2006b).

As shown in Figure 1, an electronic trigger signal provided from the laser source or laser driver is used as time trigger. Alternatively, a small fraction of the excitation laser light is reflected onto a fast photodiode that provides the stop signal for the time-domain TAC.

For the regulation of the sample temperature, the glass cuvette can be connected to a mobile cryostatic closed-loop helium system. The whole system is mobile and the optical measuring station together with the mobile cryostatic temperature regulator can be transported to any available immobile laser excitation or other experimental environment that should be studied by TWCSPC. For further details regarding the cryostatic system or the measurement configuration, see (Schmitt, 2011). Alternatively a Peltier cooling/heating system (Peltron GmbH, Germany) allows the choice of any temperature in the range of 260 K to 330 K suitable for the measurement of whole cells or sensitive preparations that should be kept at a fixed temperature. EET changes around the freezing point of the aqueous buffer solution can also be observed with the Peltier cooling. Additional applications are the investigation of the influence of cold stress in photosynthetic cells (see Schmitt et al., 2006) and decoupling effects in hybrid complexes containing semiconductor nanoparticles (CdSe/ZnS core/shell systems with dilipoic acid ligands on the surface) coupled to the PBP antenna of *A. marina* via EET (see Schmitt, 2010, 2011; Schmitt et al., 2011, 2012).

For time-resolved measurements, picosecond diode laser modules were used for excitation at 632 nm (BHL-600, FWHM 60 ps, repetition frequency 20 MHz, average intensity 100 µW/10 mm², Becker & Hickl GmbH, Berlin), 405 nm (LDH-405, FWHM 60 ps, tunable repetition frequency up to 40 MHz, Picoquant, Berlin, Germany) and 470 nm (LDH-470, FWHM 60 ps, tunable repetition frequency up to 40 MHz, Picoquant, Berlin, Germany) driven by PDL-200 or PDL-800 C (Picoquant, Berlin).

2.2. Photoluminescence emission spectroscopy

Photoluminescence excitation spectroscopy (PLE) is used to simultaneously measure the excitation and emission spectra of a sample. The excitation of the sample is scanned along the chosen spectrum, while at each wavelength section of the excitation light the corresponding fluorescence spectrum is registered. The obtained emission spectra are then plotted against the corresponding excitation wavelength as two-dimensional plots with the intensity depicted in color (see chapter 4). PLE is suitable for the illustration of EET as the uncoupled emitters typically show a fluorescence that is shifted by only a few nm (Stokes shift) to the red in respect to the corresponding absorbed excitation wavelength and, therefore, appear near the "diagonal" of the 2D-plots. If EET occurs, then the acceptor fluorescence is visible as a typical "off diagonal" element at the excitation wavelength of the donor (see chapter 4).

This principle is analogous to the so-called "off diagonal elements", which show up due to the interaction of different states due to coupling, as it would be denoted in a quantum mechanical matrix. Off diagonal elements show up when different states are coupled and effects of polarization occur.

The scheme of the PLE setup is shown in Figure 2. As light source for the excitation, a xenon lamp was used via an excitation monochromator (Kratos Schoeffel Instruments, USA) equipped with a new

grating (Thorlabs, USA). The monochromator was coupled to a stepper motor (Trinamic, Germany) controlled using a microcontroller. The fluorescence light is captured perpendicularly to the excitation beam and analyzed with a commercial precalibrated monochromator (HORIBA Jobin Yvon, France). A liquid-nitrogen-cooled CCD (HORIBA Jobin Yvon, France) was attached to the detection spectrometer to capture the spectra.

Since the CCD can only detect a part of the spectrum depending on the desired resolution, the emission spectrum has to be taken from multiple positions of the monochromator grating and composed afterwards after dark spectrum subtraction. At each scanning step, the excitation power was measured by deflecting a fraction of collimated exitation beam onto the sensor of a Thorlabs PM100USB power meter together with a Thorlabs S130VC sensor head.

For "one dimensional" time integrated measurements during excitation with a fixed wavelength a commercial USB-connected

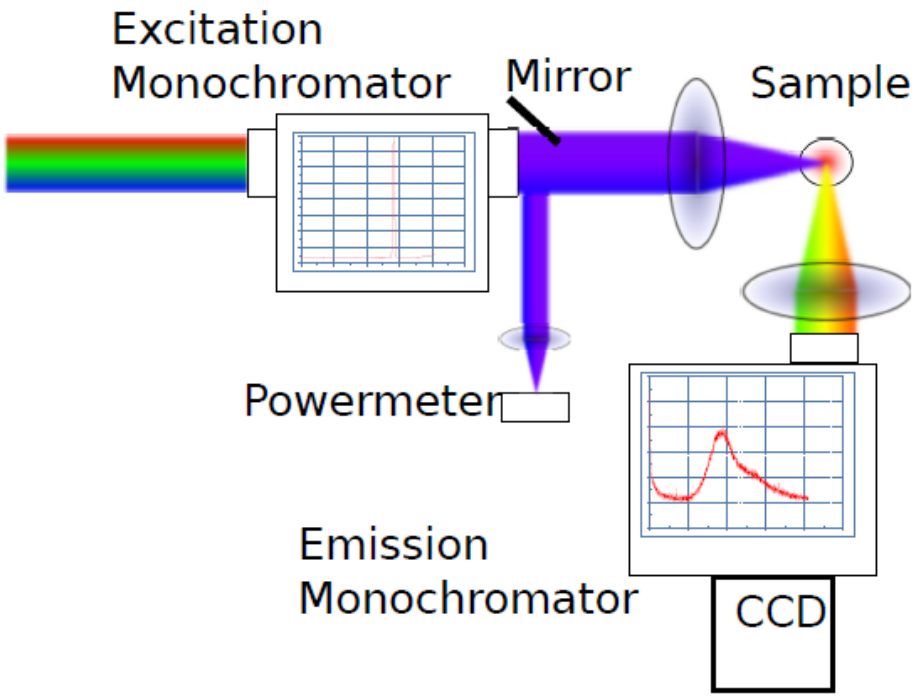

Figure 2. PLE setup used for the characterization of fluorescent proteins as shown in chapter 4. For further details, see text.

fluorometer system with CCD array (EPP2000, Scientific Instruments, Berlin, Germany) delivering a spectral resolution of 3 nm was used.

2.3. Multiparameter FLIM for simultaneous wide-field and confocal microscopy and Fluorescence correlation spectroscopy

The microscopic multi parameter setup is based on a Nikon TI Eclipse microscope as shown in Figure 3. The setup includes different light sources, excitation laser wavelengths and detectors. Fully automated optical add-ons allow to switch between different techniques like wide-field fluorescence lifetime imaging microscopy (FLIM), confocal laser scanning microscopy, total internal reflection microscopy (TIRF), 3D reconstruction tomography and fluorescence correlation microscopy (FCS). All

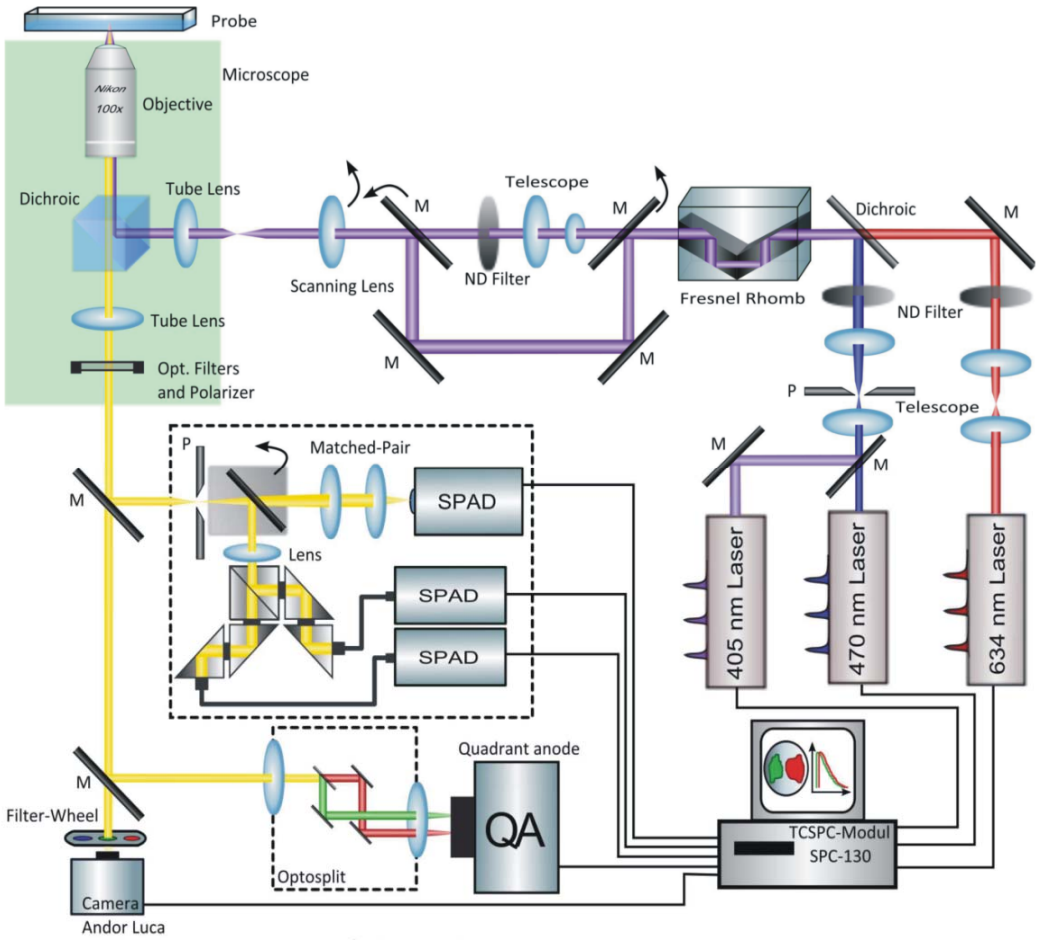

Figure 3. Scheme of the multi parameter microscopy setup, for details see text.

techniques are controllable with self-written LabVIEW-based programs via a touch screen.

FLIM and FCS in autocorrelation and cross-correlation mode can be done simultaneously. The time resolution of the setup covers a range from 10 ps to hours and is therefore suited to follow dynamics in a time regime covering 15 orders of magnitude.

For ultrasensitive wide field observations with high time and space resolution, the microscopic setup is equipped with a novel quadrant anode (QA) single photon detector with high photon throughput (up to $2*10^6$ photons/sec.) and lowest noise (< 10 photons/sec) (IfN Magdeburg, Germany).

The QA detector is equipped with a double-stage microchannel plate photomultiplier (MCP-PMT) and five separate anode elements equipped with a novel QA-Proximity-MCP-PMT-measurement head. These anode elements represent a charge division pattern comprising four planar and electrically isolated electrodes and a fifth cylindrical one surrounding the planar structure. An incident photon releasing an electron with the photocathode leads to the amplification of the electron to an avalanche along the MCP-PMT stack. The impinging electron avalanche registered on the sectorized anode is registered in analogy to the TWCSPC technique described in chap. 2.1. As the anode elements are devided into five electrodes each position of the initially registered photon on

the photocathode leads to a certain spatial distribution of the charges from the avalanche on the anode sectors. The combination of the measured charge on all five anode elements therefore allows to determine the position of the incident photon. Further details on the applied QA detection technique can be found in ref. (Vitali, 2011).

As shown in Figure 3, the fluorescence light can be optically devided by an optosplit module (Cairn Research Ltd., Faversham, UK) and, in addition, by an additional filter wheel into different color or polarization channels. The two channels from the optosplit are simultaneously registered by the QA detector. The inclusion of a filter wheel that is synchronized with the registered photon stream in the QA detection path allows a multichannel FLIM registration with up to 8 channels (2 optosplit and additional 4 synchronized channels of the filter wheel).

After hitting the anode elements, the electric charge moves to preamplifiers and is further processed by CFDs and TACs until stored into the digital register (see ref. Vitali, 2011).

According to the sample properties, the experimenter can either choose the most suitable technique or employ a combination of several options.

The setup based on the Nikon TI Eclipse microscope is arranged with different pulsed diode lasers for the excitation (LDH-405 and LDH-470 from PicoQuant Berlin; BHL-600 from Becker&Hickl, Berlin), which are collimated by two convex lenses in a telescope and cleaned spatially with a 30 µm pinhole to ensure an optimal illumination of the sample (see also chap. 2.1). For wide-field illumination it is also possible to excite the samples with a mercury lamp.

For FCS measurements, the detection pathway is equipped with a 50 µm pinhole in the image plane to block fluorescence light apart from the focal region enhancing the axial resolution. Afterwards the emission light is focused on a Single-Photon-Avalanche-Diode (SPAD). The used SPAD (MPD, Italy) has a quantum efficiency of ~40% and a time resolution of about 35 ps (FWHM). Two SPADs are employed in an additional detection path for cross-correlation spectroscopy. Fluorescence lifetime is automatically registered in the FCS mode as the arrival time of the photons is stored in absolute value and relative to the excitation laser pulse.

2.4. Data analysis

Recent progress in computational physics led to very different approaches for analysing spectral data. The fit of the decay curves in the time domain is only one approach. Inverse Laplace transformations of time- and wavelength-resolved decay curves or principal component analysis are techniques for a fully unbiased study of the measurement data. In this work, mainly the multiexponential fit of decay curves in the time domain was applied, because it allows a straightforward check of the proposed models based on rate equations for EET reactions.

The technique of single photon counting was operated with high signal to noise ratio of S/N $\sim \sqrt{S}$ > 100 in the peak channel in all measurements. With the novel QA detector (IfN Magdeburg, Germany), such S/N ratios can be achieved in measurement times of 10 min. for a FLIM picture with 2 µm spatial resolution, if the emitter is localized in the field of view (chap. 2.3). For the fluorescence setup for TWCSPC as described in chapter 2.1, such S/N ratios can be gathered in < 10 min. measurement time, if the fluorescence is spectrally localized and the lifetime is not longer than 2 ns. In fact, the exact measurement times for a desired S/N ratio depend on the spatial or spectral distribution, respectively, of the fluorescent sample and of the fluorescence lifetime, which distributes the acquired photons along the time axis.

The instrumental response function (IRF) of this system was measured to 150 ps full width at half maximum (FWHM), limiting the time resolution to about 15 ps.

New techniques using several photomultiplier tubes allow even higher count rates because pile up effects are reduced, if detector arrays containing independent detectors are used (Kim, So, 2006).

Detailed analyses of the fluorescence decay curves were performed by iterative reconvolution of a polyexponential decay model with the IRF using a global lifetime analysis minimizing the quadratic error sum χ^2 employing a Levenberg-Marquardt algorithm (for details see Schmitt et al., 2008; Schmitt, 2011; Theiss et al., 2011). The IRF was measured using destilled water as scattering medium. The multiexponential fits of all decay curves measured in one time- and wavelength resolved fluorescence spectrum were performed as global fits with common values of lifetimes τ_j (linked parameters) for all decay curves and wavelength-dependent pre-exponential factors $A_j(\lambda)$ (non-linked parameters)). The result of such a fit analysis is usually plotted as a graph of $A_j(\lambda)$ for all wavelength independent lifetimes τ_j . This plot represents the so called "decay associated spectra" (DAS) thus revealing the energetic position of individual decay components (Schmitt, 2011).

3. Excitation energy transfer, pigment-pigment and pigment-protein interaction in photosynthetic pigment-protein complexes

Photosynthesis appears to be the biosphere´s most important process in solar energy exploitation (Renger, 2008). It can be described as the light induced chemical reaction of water with carbondioxide to glucose (see Figure 4). The photosynthetic light reaction is highly endergonic and driven by Gibbs free energy of solar radiation on earth that is absorbed by green plants (for more detailed thermodynamic considerations see Schmitt, 2011).

Figure 4 and Figure 5 represent nice overviews on the hierarchical organization of higher plants. The structural organisation of photosynthetic organisms covers more than 12 orders of magnitude in space ranging from the pm-dimension of electronic orbitals up to large plants, which can be up to tens of meters in size. The dynamics covers an even wider range of up to 26 orders of magnitude in time ranging from the fs dynamics of light absorption to the life time of trees and certain plants covering thousands of years.

Figure 4 shows the typical organization of a photosynthetic tree of 10 m which is a sum of its cells (typically 10-100 μm). The single cell is the smallest organized form representing a "living system" and all higher organisms are formed by a symbiotic biosystem of such units (Heath, 1972; Lawlor, Häder, 1990; Häder, 1999). In eukaryotic organisms, the cells contain certain organelles termed chloroplasts, which are of quite variable sizes and geometries (see e.g. Häder, 1999), where photosynthesis takes place inside the thylakoid membrane. The thylakoid membrane is formed by a lipid bilayer with hydrophilic surface. Inside the thylakoid membrane, the lipophilic environment contains the membrane proteins. They are hydrophobic and therefore dissolved in the membrane as membrane intrinsic proteins.

Figure 5 shows schematically the organisation of the thylakoid membrane where the photosynthetic pigment-protein-complexes are located as membrane intrinsic proteins.

The photosynthetic reactions leading to CO_2 fixation comprise the light-driven reactions, which take place inside the thylakoid membrane, and the "dark" reactions, which take place inside the chloroplast stroma (indicated as a red cycle process in Figure 5).

The thylakoid membrane divides the aqueous phase of the chloroplasts into the thylakoid lumen and the chloroplast stroma. Protons released into the thylakoid lumen and protons transferred from the stroma into the lumen form a transmembrane electrochemical potential difference. This drives the adenosine triphosphate (ATP) synthase that phosphorylates adenosine diphosphate into the energy-rich ATP compound required as free energy source in the dark reaction for carbon reduction.

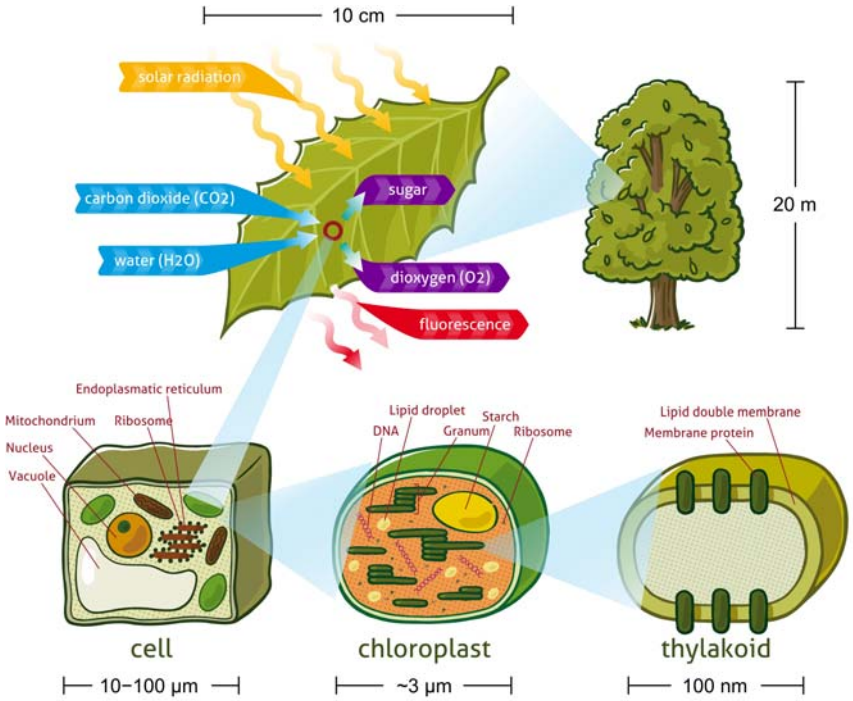

Figure 4. Hierarchic structures of green plants as published in ref. (Schmitt, 2011). The chloroplasts contain the Grana stacks of the thylakoid membrane where photosynthesis takes place. Figure provided by Florian Schmitt (Florian Schmitt Illustration).

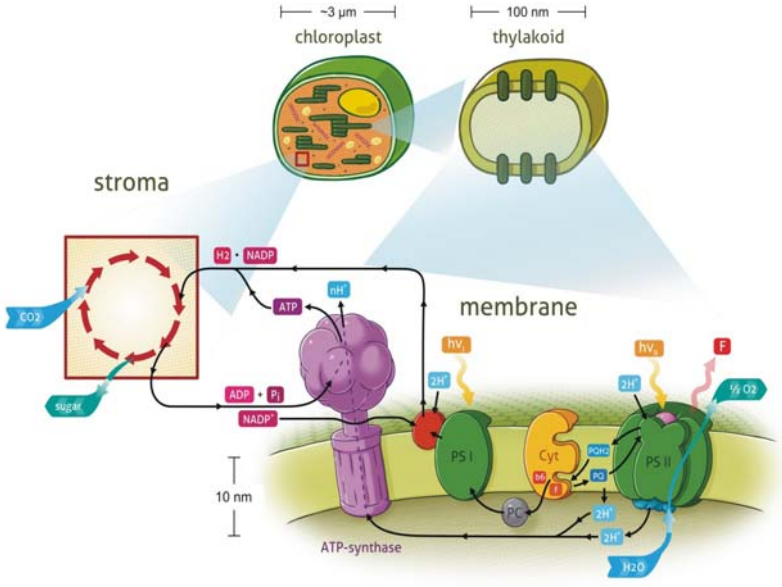

Figure 5. Membrane proteins inside the lipid double layer of the thylakoid membranes as published in ref. (Schmitt, 2011). Figure provided by Florian Schmitt (Florian Schmitt Illustration). For further details see text.

The "light" reaction performs the exploitation of solar energy by highly functionalized PPCs. Solar energy represents the unique Gibbs free energy source of earth´s biosphere. The Gibbs free energy is converted into high energy chemical compounds via the process of photosynthesis. This is perfectly achieved by incorporation of suitable chromophores into protein matrices. The PPCs are optimized towards energy absorption and transfer in order to produce the high-energy compounds ATP and NADPH.

The "light" reaction performs the exploitation of solar energy by highly functionalized PPCs. Solar energy represents the unique Gibbs free energy source of earth´s biosphere. The Gibbs free energy is converted into high energy chemical compounds via the process of photosynthesis. This is perfectly achieved by incorporation of suitable chromophores into protein matrices. The PPCs are optimized towards energy absorption and transfer in order to produce the high-energy compounds ATP and NADPH.

Two classes of pigment-protein complexes have developed in evolution with distinctly different functions: antenna systems and reaction centers (RCs) (see Ke, 2001). These operational units perform the light-driven processes of photosynthesis in a controlled and highly efficient manner: The pigments of the antenna complexes (for reviews, see Green, Parson, 2003; Renger, 2008) absorb light and transfer the electronic excitation energy via radiationless EET to the photochemically active pigment(s) of the RCs, where they are transformed into electrochemical free energy (for a review, see Renger, 2010).

The electronically excited singlet states formed by light absorption of the Chl molecules are not completely transformed into Gibbs free energy. A fraction is emitted as red fluorescence that serves as a fingerprint of the excited states and their dynamics (see Schatz et al., 1988).

Interestingly, both coupling schemes play an important role in photosynthesis and sometimes one of these schemes clearly dominates in the determination of the EET properties: i) the pigment-pigment coupling, which is the dominating EET pathway for example in the LH2 of purple bacteria (Freer et al., 1996; Ketelaars et al., 2001; Park, Schulten, 2001; Scheuring et al., 2001; Schulten, 2001; Renger and Kühn, 2007), and ii) the pigment-protein interaction well known to represent the main driving force to generate an energy funnel towards the reaction center in the Fenna-Matthews-Olson complex of green sulfur bacteria (Adolphs, Renger, 2006; Müh et al., 2007; Wen et al., 2011). In most photosynthetic complexes, an interplay of both processes determines the EET processes.

The enhancement of the absorption cross section of the photosystems and the efficient transfer of electronically excited energy is only one function of photosynthetic antenna complexes. In addition, they have regulatory functions like the dissipation of excess energy to avoid the generation of singlet oxygen at high-light conditions (see Häder, 1999 for an overview).

The structural arrangement of the pigments and the fine tuning of the Chl molecules by the environment lead to a directed energy transfer from the antenna to the photochemically active reaction center (RC). The absorbed light energy is able to bridge distances of 30 nm to the RC with up to 99 % quantum efficiency (Häder, 1999).

In contrast to the common architecture of the RC, the antenna structures are found to vary in different photosynthetic organisms. The exact pigment composition of the antennae is not completely determined for a certain species but depends on the growth conditions, light intensity and light quality during growth. The latter effect is known as chromatic adaptation. A detailed overview on the different complexes is found in ref. (Häder, 1999).

Time- and wavelength-correlated single photon counting measurements were performed on preparations of photosynthetic pigment-protein complexes (PPC) (Schmitt et al., 2006; Theiss et

al., 2008), whole cells of different cyanobacteria, especially the unusual cyanobacterium *A. marina* discovered in 1996 (Petrášek et al., 2005; Schlodder et al., 2007; Schmitt, 2011; Schmitt, 2010; Schmitt et al., 2006; Theiss et al., 2008) and the water-soluble chlorophyll binding protein (WSCP) genetically expressed in *E. coli* and reconstituted with Chl *a*, Chl *b* or mixtures of Chl *a* and Chl *b* (Theiss et al., 2007; Schmitt et al., 2008), higher plants like *Arabidopsis thaliana* (Belyaeva et al., 2011) and whole cells of the green algae *Chlorella pyrenodoisa chick* (Belyaeva et al., 2008) to study energy transfer and electronic relaxation in systems of coupled pigments interacting with the local protein environment.

The accuracy of the newest findings suggests that the terminus "picobiophotonics" seems to be more accurate to describe the biophysical research at the edge of the achievable resolution (Schmitt, 2011). *A. marina* is exemplarily chosen as prominent example of picobiophotonic studies, as it is up to date the only known organism which mainly contains Chl *d* instead of Chl *a* in the membrane-intrinsic Chl antenna (Miyashita et al., 1996). This makes *A. marina* an interesting object that is unique in its structural organisation of the rod-shaped membrane-extrinsic phycobiliprotein (PBP) antenna (Marquardt et al., 1997; Hu et al., 1999; Mimuro et al., 1999). Since cyanobacteria containing PBP complexes organized as phycobilisomes (PBS) are well studied, the results obtained on the PBP antenna of *A. marina* can be compared with the PBS properties in a straightforward fashion (Glazer, 1985; Gillbro et al., 1985; Holzwarth, Suter, 1987; Holtzwarth, 1991; Mullineaux, Holzwarth, 1991; Sharkov et al., 1994; Debreczeny et al., 1995a, 1995b; Trissl, 2003). A wide range of spectroscopic techniques was applied that allowed the determination of EET processes in the unique rod-shaped phycobiliprotein antenna and from the PBP antenna to the Chl *d* containing core complex (Petrášek et al., 2005; Schmitt et al., 2006; Theiss et al., 2008) as well as the composition of the PS I (Hu et al., 1998) and PS II (Schlodder et al., 2007).

3.1 Excitation energy transfer in the PBP antenna of *A.marina*

The antenna complexes of photosynthetic organisms enhance and regulate the effective absorption cross section by connecting a huge number of pigments to the RC as well as by regulating the connectivity and excited state lifetime. The modulation by the protein environment and the coupling of the pigments determines the probability distribution of EET pathways. Additionally, the high number of non-degenerated states of all pigments in these antenna complexes enables light absorption in a wider spectral range than by single pigment molecules.

In photosynthetic organisms, different pigment molecules are bound to peripheral antenna complexes which close the absorption gap of the chlorophyll molecules in the green spectral range and therefore raise the efficiency of the antenna. Such pigments are carotenoids in LHCII and phycobiliprotein (PBP) complexes containing phycoerythrin (PE), phycocyanin (PC) and allophycocyanin (APC) in cyanobacteria. The phycocyanobilin pigments are open porphyrine ring systems exhibiting strong absorption in the green and yellow spectral range thus being responsible for the blue colour of cyanobacteria. Figure 6 shows the absorption spectrum of the PBP antenna of *A. marina* that contains hexamers of PC and APC and an additional heterohexamer composed of an APC and a PC trimer.

Cyanobacterial phycobilisomes (PBS) (Gillbro et al., 1985; Glazer, 1985; Holzwarth, Suter, 1987; Häder, 1999; Trissl, 2003; Schmitt, 2011) are composed of PC and APC trimers and tend to aggregate further in the so-called „face-to-face" dimerisation forming hexameric structures (for further detail see e.g. Glazer, 1985; Holzwarth, Suter, 1987; Theiss, 2006).

These hexamers undergo a further aggregation forming so-called PBP antenna rods which aggregate to huge (up to 50 nm in diameter)

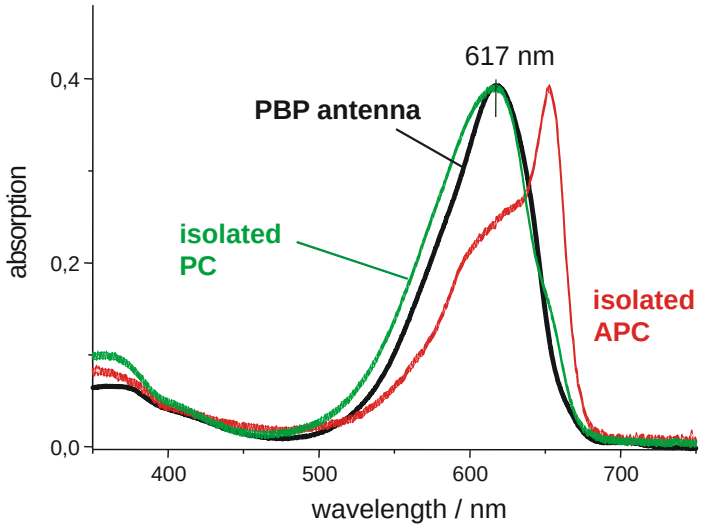

Figure 6. Absorption spectrum of PBP isolated from the cyanobacterium *A. marina* (black curve) in comparison to isolated PC trimers (green line) and isolated APC trimers (red line) redrawn from Theiss (2006). The trimers were diluted in buffered aqueous solution.

phycobilisomes (PBS) as shown in Figure 7 (left side). In Figure 7, the APC-containing hexameric structures seem to be present only in form of single discs, but they are also found to form rod-shaped staples of hexameric discs, which are interacting with the outer thylakoid membrane.

Some cyanobacterial PBS additionaly contain phycoerithrin (PE) in addition to PC and APC hexamers in the PBS.

The properties of PBS are well understood and, therefore, PBS are quite a good system for reference measurements of energy transfer processes. In the study presented here, published results of PBS mainly from the cyanobacterium *Synechocystis sp. PCC 6803* containing PC and APC as schematically shown in Figure 7 were compared with results obtained on the PBP antenna of *A. marina.*

In Schmitt (2011), our measurements confirmed that energy migrates within about 200 ps from PC to Chl *a* in *Synechocystis*, which is a typical value for PBS of common cyanobacteria in agreement with Holtzwarth and Suter (1987), Trissl (2003) and Glazer (1985).

It is assumed that the PBS are mainly associated with the PS II core complex of the thylakoid membrane. Most cyanobacteria contain high amounts of PBS, which makes the PBS chromophores the most important light-harvesting pigments found in cyanobacteria. PBS undergo state transitions from PS II to PS I.

The PBPs of *A. marina* are of much simpler structure than PBS and have been reported to consist of four hexameric units (Marquardt et al., 1997; Mimuro et al., 2004) (see Figure 7, right side). Each homohexamer covalently binds 18 PCB molecules as chromophores. The PC/APC heterohexamer is found to contain 9 PCB and 6 APCB chromophores. Isolated PBPs from *A. marina* exhibit a fluorescence maximum at 665 nm (APC) with a shoulder at about 655 nm (PC) at room temperature (Marquardt et al., 1997; Mimuro et al., 2004).

In our studies, the PBP structure suggested by Marquardt et al. (1997) was confirmed by transmission electron microscopy of the PBP antenna complexes of *A. marina*, as shown in Figure 8. The contrast of the protein structure in the electron beam is low. Therefore, a procedure of

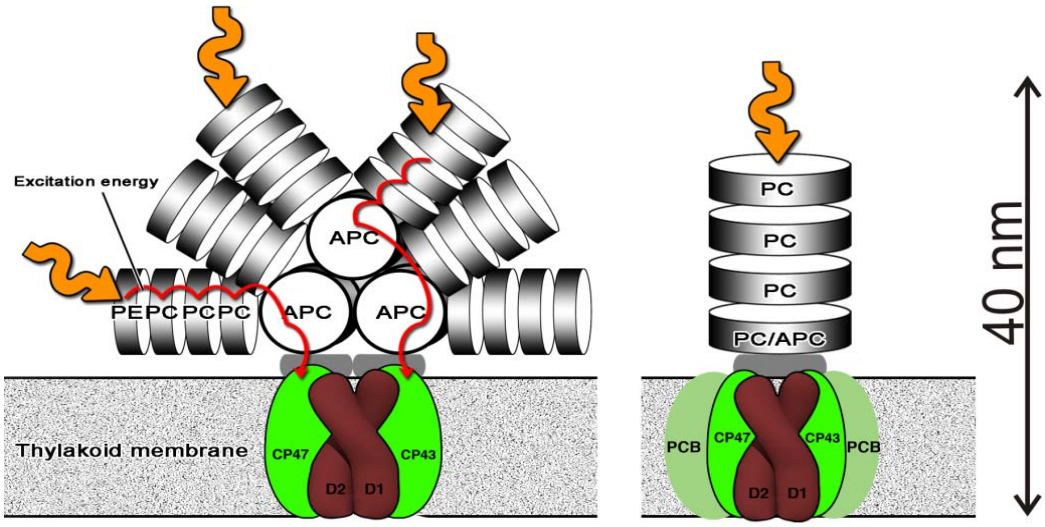

Figure7. Overall geometry of PBS found in cyanobacteria (left side) and rod-shaped PBP antenna structure of *A.marina* (right side) according to Marquardt et al. (1997), figure as published in Schmitt (2011). Both PBP contain PC and APC. In the PBS, PE is found additionally.

negative staining had to be performed to achieve a picture of the PBP structure as described in Schmitt (2011).

The experimental results summarized in ref. (Schmitt, 2011) showed that in the PBP antenna of *A. marina*, ultrafast energy equilibration occurs between different PC molecules (< 1 ps), which are bound to a hexameric protein structure, followed by the equilibration between the PC and the APC containing hexamers with a time constant of 3-5 ps (Theiss et al., 2008). A subsequent relaxation of the excitation energy from PC and APC containing hexamers of the membrane-extrinsic PBP antenna to spectrally red-shifted APC molecules, which are most probably located in the linker protein, was resolved to 20 (+/- 10) ps (Schmitt et al., 2006).

The single EET steps with molecular resolution according to the results of a theoretical analysis of the coupling led to the concept that single specific molecules are involved in the corresponding EET and/or exciton relaxation process. The results are summarized in Theiss (2006) and Theiss et al. (2011).

In whole cells of *A. marina*, the energy transfer between the PBP antenna and the Chl *d* containing membrane intrinsic antenna complex was found to occur within an additional 50 ($^{+}$/- 5) ps transfer step, as published previously (Petrášek et al., 2005). Therefore, the excitons reach the reaction centre inside the membrane-intrinsic Chl *d* complexes within 70 ps in *A. marina*. This value is three times faster than in typical cyanobacteria containing bigger PBP and Chl *a* containing antenna complexes (Petrášek et al., 2005). For redox potential of cofactors in *A. marina,* see (Allakhverdiev et al., 2010, 2011; Tomo et al., 2011).

Therefore, we performed simulations of the exciton diffusion within the simpler rod-shaped structures of *A. marina* in comparison to the more complex PBP structures of other cyanobacteria (Schmitt, 2011). The time-resolved fluorescence data is fitted

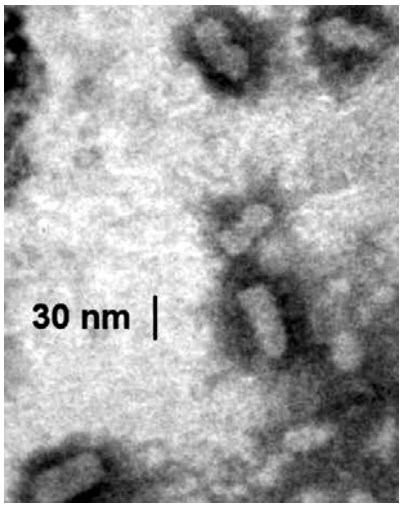

Figure 8. Electron microscopic study of PBP preparations of *A. marina* in buffer containing phosphate after negative staining with $Na_4[W_{12}SiO_{40}]$. The PBP antenna complexes appear transparent (white) due to the process of negative staining, while the staining salt leads to a dark grey contrast. The figure was published in Schmitt (2011).

and afterwards plotted in form of decay-associated spectra (DAS), which are in detail described in chapter 2.4 and ref. (Schmitt, 2011). A result of the measured DAS compared to the results from a simulation according to rate equation models described in Schmitt (2011) is shown in Figure 9.

These simulations showed that entropy effects and the neighbouring energetic states of PBP in comparison to Chl *a* result in comparably small exciton diffusion coefficients while the small size of the *A. marina* antenna leads to fast energy transfer in comparison to the big PBS. Figure 10 summarizes the single EET transfer steps that lead to an agreement between measured data (Figure 9, left side) and the simulated DAS (Figure 9, right side) obtained from an evaluation of a rate equation model involving the transfer steps shown in Figure 10.

The distance of the terminal emitter of the PBP antenna in *A. marina* and the nearest Chl *d*

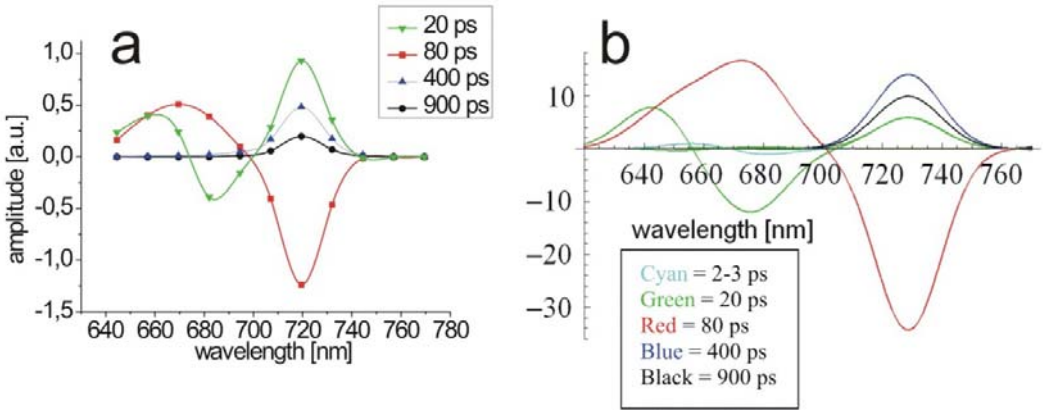

Figure 9. a) measured DAS of *A. marina* after excitation with 632 nm at room temperature. The simulated DAS is shown in panel b). The graphics was published in Schmitt et al. (2010).

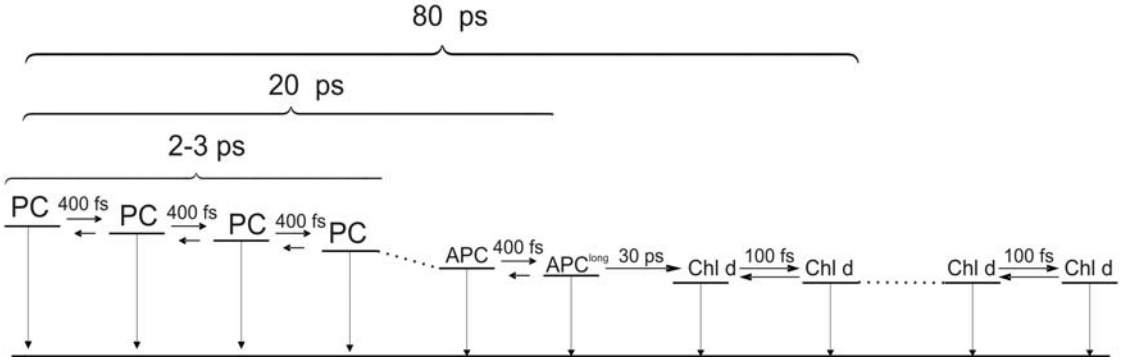

Figure 10. Scheme for simulating the data presented in Figure a). The simulated DAS are shown in Figure b). The Figure was published in Schmitt (2011).

molecule was determined to 3.3 (+/- 0.3) nm according to the theory of Förster resonance energy transfer. This distance changes at 0°C lead to a decoupling of the PBP antenna from the membrane-intrinsic Chl *d* antenna (Schmitt et al., 2006), which might enable temperature-switchable coupling. The mechanism could help to construct intelligently switchable light-harvesting systems.

A more structure-related overview on the results obtained by the investigation of the PBP antenna of *A. marina* in comparison to the EET transfer steps in PBS from a typical cyanobacterium (*Synechococcus* 6301) is shown in Figure 11.

3.2. Pigment-pigment and pigment-protein interaction in water-soluble chlorophyll binding protein

Reaction centers and most light harvesting complexes, the two types of pigment-protein complexes that are found in photosynthetic organisms, are highly hydrophobic and incorporated into the thylakoid membrane as integral proteins.

In addition to these operational units of the photosynthetic apparatus, many plants (Brassicaceae, Polygonaceae, Cheno-podiaceae and Amaranthaceae) contain another type of chlorophyll-binding protein that are water-soluble and not bound to thylakoids. These highly hydrophilic chlorophyll proteins are denoted water-soluble chlorophyll proteins (WSCPs) (see ref. (Schmitt et al., 2008) for more details on WSCP).

The WSCP family is divided into two classes, Class I giving rise to a red shift of the absorption spectrum upon photoillumination (photoswitchable class) and class II, which remains spectrally invariant (for a review on WSCP see Satoh et al., 2001). Upon pigment binding, the WSCPs tend to form tetramers or higher oligomers (Satoh et al., 1998; Schmidt et al., 2003).

Up to date, the functional role of the WSCPs is not yet clarified. Interestingly, the WSCP expression is stimulated by different types of stress like drought (Downing et al., 1992), salinity (Reviron et al., 1992), heat (Annamalai, Yanagihara, 1999), or leaf detachment (Nishio, Satoh, 1997). The water solubility and localization of WSCP in the plant makes it unlikely that WSCP is involved in the photosynthetic process. Moreover, one can speculate on a protective role against degradative processes of the photosynthetic apparatus or transport of chlorophyll molecules during stress situation (e.g. in winter). This assumption is underlined by taking into account the high affinity for chlorophyll binding (Satoh et al., 1998; Schmidt et al., 2003). Therefore, one might speculate on a regulatory role in controlling pigment synthesis or decay pathways, thus avoiding or diminishing

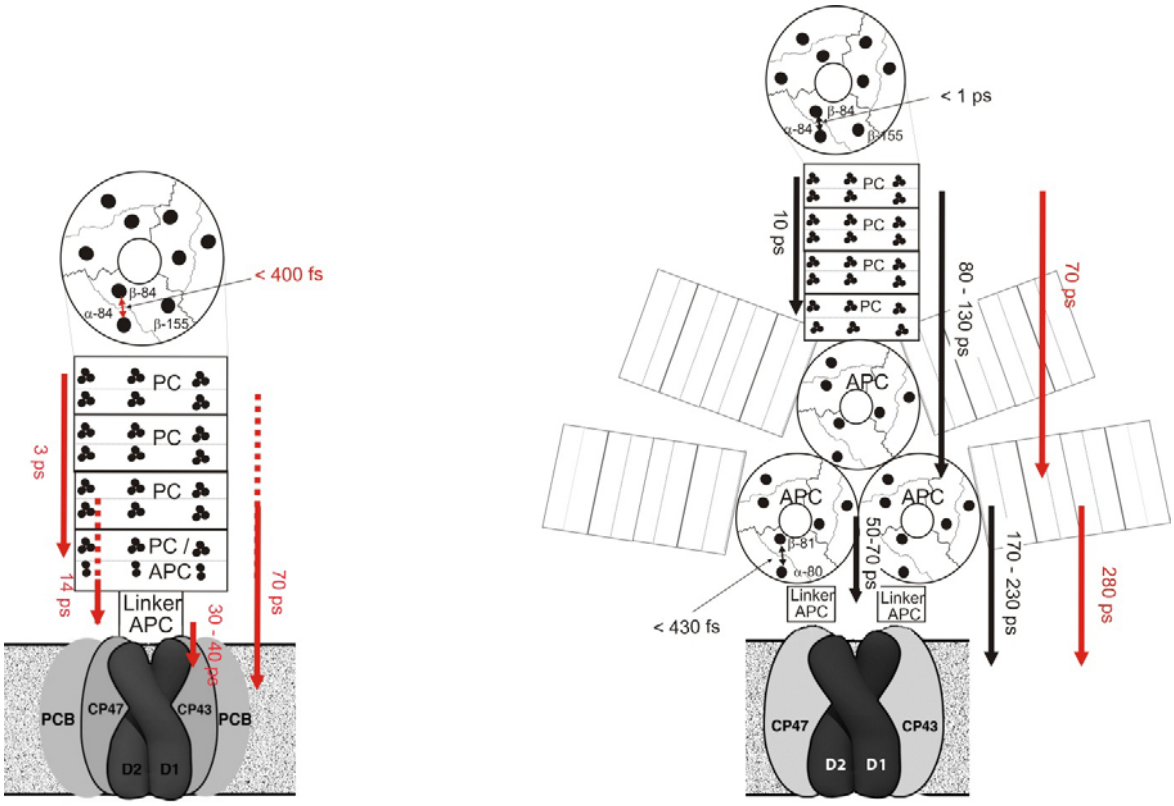

Figure 11. Kinetics of excitation energy transfer (EET) processes in *A. marina* and in the cyanobacterium *Synechococcus* 6301 as published in Theiss et al. (2011). Left panel: Model scheme for of the excitation energy processes (EET) within the PBP antenna rod and between the PBP antenna and Chl *d* in a *A. marina*. At the top, the model scheme of the PC trimer with its bilin chromophores is shown. Right panel: Model scheme and time constants for the EET within the phycobilisomes of Synechococcus 6301 and from there to the RC giving a resúmé of the literature (Gillbro et al., 1985; Holzwarth, Suter, 1987; Holzwarth, 1991; Mullineaux, Holzwarth, 1991; Sharkov et al., 1994; Debreczeny et al., 1995a, 1995b).

deleterious photodynamic effects of the chlorophyll triplets formed by irradiation. A support of this proposal might be the finding that a WSCP homologue from barley (Hordeum vulgare) is able to bind chlorophyllide in chloroplasts after exposure of etiolated seedlings to light (see ref. Schmitt et al., 2008).

Regardless of the detailed function of WSCP, it seems clear that the mode of chlorophyll binding to the protein matrix is an essential parameter for the type of function. This, together with the rather simple pigment arrangement of two (max. four) Chl molecules in a strongly excitonic coupled dimeric structure, makes WSCP ideally suited for the selective analysis of pigment-protein and pigment-pigment coupling in chlorophyll binding proteins.

Detailed spectroscopic studies and theoretical analysis of WSCP helped to resolve the structural arrangement of the chlorophyll molecules in recombinant class II a WSCP from cauliflower reconstituted with different chlorophylls (Chl *a*, Chl *b* or mixtures of both) (see ref. Theiss, 2006; Theiss et al., 2007; Renger et al., 2007, 2009, Renger et al. 2011; Schmitt et al., 2008; Pieper et al., 2011; Schmitt, 2011). The combined efforts employing various experimental techniques and theory finally

lead to the conclusion that the mentioned WSCP binds the pigments in form of an excitonically strongly coupled dimer with an "open sandwich" geometry suggesting an open sandwich configuration with a tilt angle of about 30° for Chl *a* homodimers, Chl *b* homodimers and Chl *a* / Chl *b* heterodimers in WSCP (Renger et al., 2009, Renger et al. 2011; Theiss et al., 2007). It was very exciting to see that the first published X-ray diffraction crystal structure of a Class II WSCP at 2.0 Å resolution (Horigome et al., 2007) shows Chl binding in the predicted open sandwich geometry with a tilt angle of 27°. In the following years, the determination of the energetic levels of the upper excitonic state in the coupled Chl dimer within the protein matrix was completed by the finding that two protein configurations modulate the bound, strongly coupled dimer (Theiss et al., 2007; Pieper et al., 2011). Together with the theoretical results (Theiss, 2006; Theiss et al., 2007; Renger et al., 2007, 2009), the model consistently describes the fast excited state dynamics observed in Chl *a* / Chl *b* heterodimers on the fs and ps time scale (Theiss et al., 2007) and the rather complex temperature dependency of the time-resolved fluorescence dynamics on the ps and ns time scale (Schmitt et al., 2008; Renger et al., 2009, 2011; Schmitt, 2011).

The fact that WSCP exhibits an unusual high photostability of bound chlorophyll dimers is not clarified in full detail yet (Satoh et al., 2001; Schmidt et al., 2003). In the literature, it is speculated that the protein environment forms a diffusive barrier for oxygen and therefore prevents the reaction between Chl triplet states and oxygen triplets to highly reactive singlet oxygen (Hughes et al., 2006).

The question is how the interplay of pigment-pigment and pigment-protein interaction determines the fluorescence dynamics on the ps and ns time scale and how combined complementary techniques helped to resolve this problem:

The fluorescence dynamics of WSCP exhibits three time constants at deep temperatures (10 K) (for details, see ref. Schmitt et al., 2008; Renger et al., 2011; Schmitt, 2011), which can be explained by a distribution of pigment-pigment interactions and pigment-protein interactions (Schmitt et al., 2008). From the data of femtosecond absorption spectroscopy (Theiss, 2006; Theiss et al., 2007), the distance of the two coupled Chl molecules in WSCP could be determined to be 0.74 nm (Renger et al., 2007).

The fluorescence and absorption dynamics and especially the complex temperature dependency of the observed fluorescence dynamics can well be explained by strong pigment-pigment coupling of the chlorophyll dimer in the open sandwich geometry, which is modulated by a strongly temperature-dependent protein environment.

While at a first glance these results obtained mainly from deep temperature time-resolved fluorescence spectroscopy appeared rather qualitative, the exact determination of the energetic levels of the upper excitonic state in the coupled Chl dimer within the protein matrix was possible by site selective hole burning spectroscopy (Pieper et al., 2011). Pieper et al. could not only distinguish the upper and lower excitonic state as found in absorption, transient absorption spectroscopy and well explained by theory (Theiss, 2006; Renger et al., 2009; Theiss et al., 2007), but the authors found an energetically "higher" and "lower" protein configuration for each excitonic state. This term scheme as shown in Figure 12 was finally suitable to explain the rather complex temperature dependency of the time-resolved fluorescence dynamics. The details of these results are published in ref. (Renger et al., 2009, Renger et al. 2011) and (Schmitt, 2011).

The conclusions from our analysis combining the mentioned results show that reconstituted recombinant class II a WSCP from cauliflower offers a most suitable sample material for detailed studies on pigment-pigment and pigment-protein interactions, since the small number of two strongly coupled Chl molecules modulated by the local protein environment mainly by two prominent configuration states is the most simple system conceivable that comprises both: pigment-pigment

and pigment-protein interaction. The successful theoretical analysis of this system confirms the strength of such a reduced model system that allows the consolidation of various experimental findings into a synergistic and unambiguous model.

For possible applications, the shielding towards interaction of O_2 with Chl molecules bound to the WSCP protein matrix is a very attractive feature that opens a way for systematic studies on tunable barriers for oxygen diffusion. WSCP can be expected to become a highly interesting system for future research.

The reconstituted WSCP is formed from the recombinant apoprotein and chlorophyll molecules in solution and, therefore, modification of the protein or the chromophores is conceivable. The diffusion barrier could be selectively modified in order to achieve tunable interaction between O_2 and Chls or other pigments.

The high stability of WSCP is only observed in its tetrameric form, in which the protein protects the bound Chl from photodegradation.

Switchable changes of the structural integrity might be used to destabilize the protein tetramers and to enhance the photodynamic activity of WSCP. One possibility to achieve this goal might be the assembly of WSCP with photoactive groups that trigger light-induced structural changes (e.g.

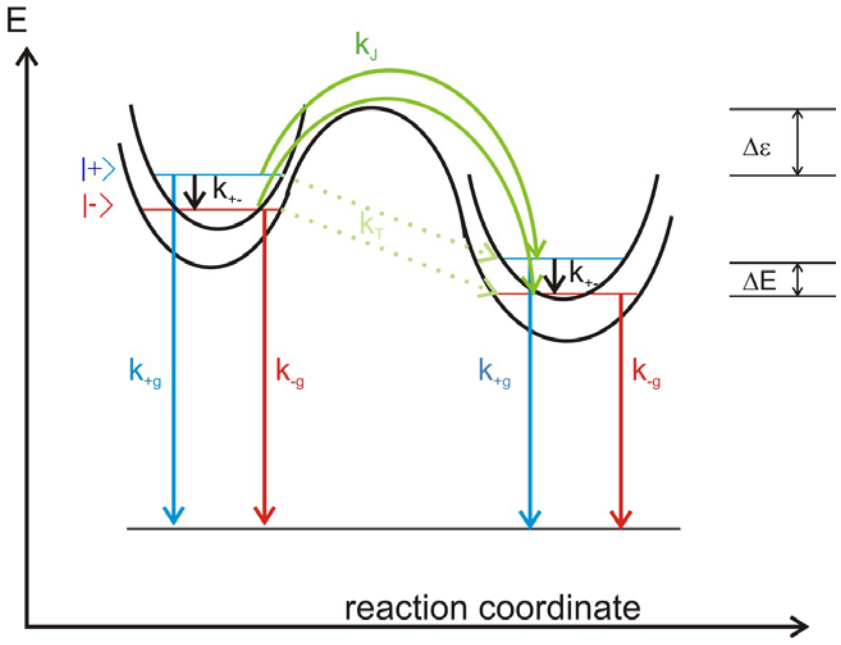

Figure 12. Extended model of the potential curves for the excitonic states modulated by the protein environment in water-soluble chlorophyll binding protein (WSCP), as published in Schmitt (2011). The two excitonically split states $|-\rangle$ (red) and $|+\rangle$ (blue) are localized in form of parabolic potentials in each protein configuration. The excitonic relaxation from $|+\rangle$ to $|-\rangle$ occurs with the rate constant k_{+-} (black arrows) while the electronic relaxation to the ground state occurs with the time constant k_{+g} from the upper excitonic level $|+\rangle$ (blue arrows) and with the rate constant k_{-g} from the lower excitonic level $|-\rangle$ (red arrows). The relaxation from one parabola to the other is assumed to occur via a tunneling process k_T (light green) or via the thermally activated channel k_J (dark green).

cis/trans isomeric forms), thus changing the diffusion barrier to O_2 in a controlled manner. A combined mutagenesis with a selection strategy might be used to achieve these properties by an evolutionary process. Alternatively, structural changes could lead to the release of Chl, thereby stimulating enhanced singlet oxygen formation and creating a strong ROS sensitizer.

3.3. Studies on the EET between semiconductor nanocrystals and PBP complexes from *A. marina*

The targeted design of the optical properties of artificial and particularly biomimetic systems will lead to innovative units with high efficiency of light absorption and directed EET. Such systems are believed to be most promising as hybrid systems for artificial photosynthesis, for example consisting of highly absorbing nanostructures and photosynthetic reaction centers or formed by biological light harvesting systems functionally coupled to solar cells.

The external power conversion efficiency after immobilization of photosynthetic reaction centers (RCs) on electrodes is rather low mainly for two reasons:

a) electron transfer (ET) between RC and electrode is hampered due to localization of ET cofactors inside the protein matrix, thus giving rise to a rather long electron tunneling distance and
b) the optical density of the monolayer of RCs immobilized on the electrode surface is very low (about 0.01) and, therefore, the light capture efficiency is negligibly small.

In addition, hybrid complexes of photosynthetic subunits and artificial nanostructures are unstable due to degradation processes of pigment-protein complexes.

These problems have to be solved for using pigment-protein complexes as parts of electronic devices.

QDs that were functionalized at the surface with acidic groups interact electrostatically with proteins and can serve as efficient artificial donors and acceptors in hybrid systems consisting of QDs and proteins. EET, ET reactions and protein reorganization in these hybrid systems were studied experimentally and analyzed within the framework of theoretical models of rate equations.

We have started investigations on the mechanisms of interaction between various chromophor-protein complexes and semiconducting CdSe/ZnS and CdTe nanocrystals denoted as quantum dots (QDs), as exemplified in the following according to our publications (Schmitt, 2010, 2011; Schmitt et al. 2011, 2012). It was shown that QDs can form efficiently coupled hybrid structures with PBP antenna complexes from *A. marina*. The efficiency of EET can reach values of up to 90 % (Schmitt et al., 2011, 2012).

In the described hybrid systems, the quantum dots (CdSe/ZnS) function as donors of electronic excitation energy, whereas PBP complexes serve as acceptors. Kinetics and efficiency of EET from QDs to photosynthetic pigment-protein complexes are monitored by using time-resolved fluorescence spectroscopy.

Figure 13 presents a schematic view of the PBP antenna of *A. marina* and the structure of the QDs used in this study. For the detailed structure and electronic properties of these QDs, see also (Medintz, Mattoussi, 2009) and (Bawendi et al., 1992) and references therein. The description of EET processes inside QDs modelled by rate equations is found in ref. (Bawendi et al., 1992).

The overall structure of the QDs used in this study is schematically shown on the right side of Figure 13. The QDs consist of a Cd/Se core of 3.3 nm diameter and a ZnS shell which is functionalised at the surface by dihydrolipoic acid ligands that are negatively charged in solution at pH 7. The chemical composition of these QDs is thoroughly described in ref. (Medintz, Mattoussi, 2009).

The left panel of Figure 14 shows the fluorescence decay curves of the 530 nm emission from the QDs

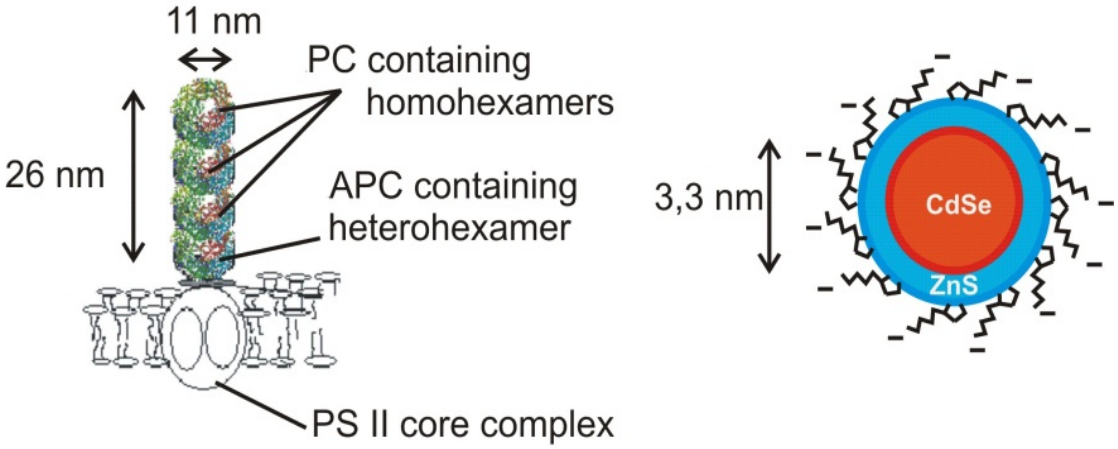

Figure13. Scheme of the organisation of the PBP antenna in *A.marina* (left side) and structure of the CdSe/ZnS-530-QDs with fluorescence maximum at 530 nm (right side) used in this study as published in Schmitt et al. (2011).

at room temperature in the absence (black curve) and presence (red curve) of isolated PBP antenna rods from *A. marina* (see Figure 14, left side).

The right panel shows the fluorescence decay at 660 nm from PBP antenna complexes in the absence (black curve) and presence (red curve) of CdSe QDs as published in ref. (Schmitt, 2011).

The drastically accelerated decay of the 530 nm emission from the QDs is concomitant with the decrease and increase of the 530 nm and 660 nm emission, respectively, of the integrated fluorescence from QDs and PBPs. This is indicative of a strong quenching of the QD fluorescence by coupled PBPs from *A. marina*. This pronounced effect reflects a highly efficient EET from the QDs to the PBPs. The PBP fluorescence, on the other hand, shows a characteristic "rise kinetics", which leads to a temporal shift of the fluorescence maximum when energy is transferred to the PBP from a donor state (see red curve in Figure 14, right side). After fitting the decay curves with exponential components, such rise kinetics shows up as a negative amplitude (negative exponential function with typical time for the energetic "rise") in the decay-associated spectra (DAS).

The comparison of the PBP decay curves of samples in the absence (Figure 14, right side black curve) and presence (Figure 14, right side, red curve) of QDs shows that the PBP luminescence maximum after excitation is completely shifted towards longer times in presence of QDs (red curve) in comparison to the emission of pure PBP (black curve). This is a clear indication for an efficient EET.

Time-integrated and time-resolved fluorescence measurements at different temperatures were performed to analyse the time constants of EET between PBP complexes and the QDs in the hybrid complexes as a function of the temperature.

Figure 15 shows time-integrated emission spectra at different temperatures of the hybrid system containing QDs and PBP and the absorption spectrum of the PBPs which remains virtually invariant with respect to temperature in the investigated range (data published in ref. (Schmitt et al., 2011)).

At 273 K, the intensity of the integrated red PBP luminescence exceeds the integrated green QD luminescence (see right side of Figure 15). In samples cooled down to below 273 K (the

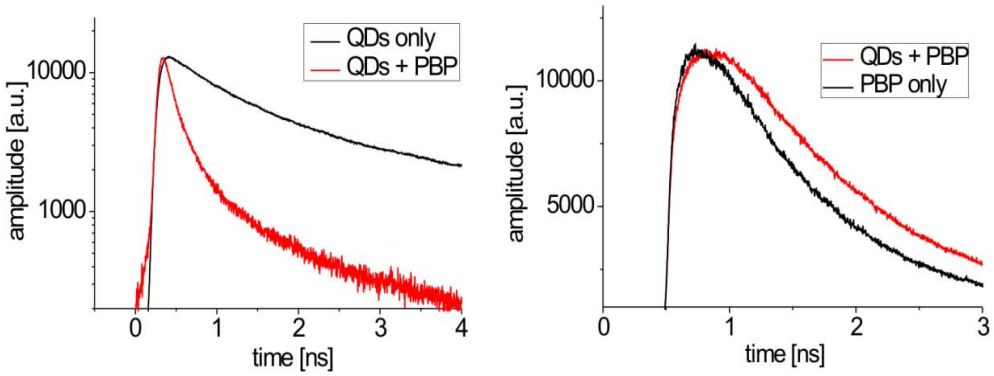

Figure 14. left side: Time course of the fluorescence emission at 530 nm from CdSe-530 QDs after excitation with 405 nm laser pulses (60 ps FWHM) at room temperature in buffer solution in the absence (black curve) and presence (red curve) of isolated PBP antenna rods of *A.marina*. Right side: Time course of the fluorescence emission at 660 nm from isolated PBP antenna rods of *A.marina* after excitation with 405 nm laser pulses (60 ps FWHM) at room temperature in the absence (black curve) and presence (red curve) of CdSe-530 QDs. All decay curves are normalized as published in Schmitt (2011).

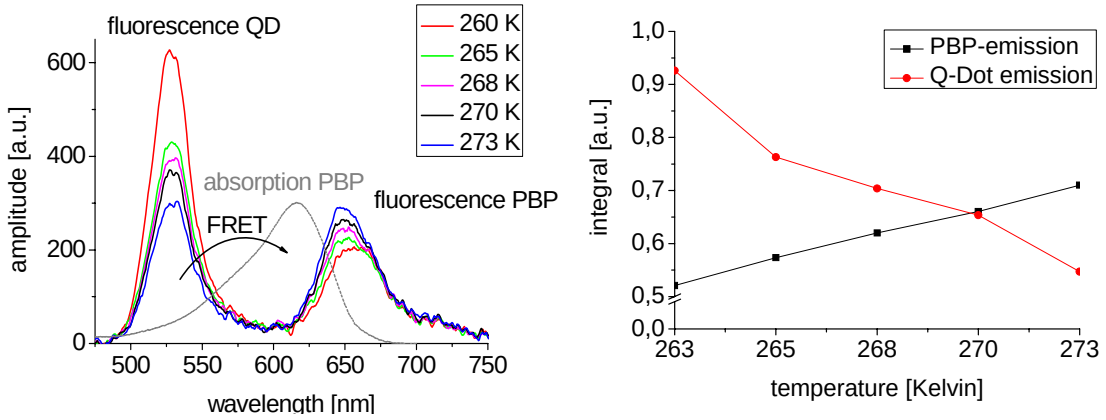

Figure 15. Left side: Time-integrated fluorescence spectrum of the hybrid systems containing CdSe/ZnS-QDs and PBP antenna complexes at different temperatures after excitation with 405 nm laser pulses and absorption spectrum of the PBPs at room temperature (grey, dashed line). Right side: integral of the fluorescence spectrum of CdSe QDs (500-560 nm, red curve) and PBP antenna complexes (600-710 nm, black curve) at different temperatures. Graphics have been published in Schmitt et al. (2011).

freezing point of the solution containing QD-PBP hybrid point of the solution containing QD-PBP hybrid complexes is about 270 K), the integrated fluorescence of the QDs continuously increases at the expense of the PBP luminescence with decreasing temperatures (see right side of Figure 15). This effect is fully reversible, i.e. during warming up to 273 K the pronounced peak at 530 nm of the fluorescence spectrum decreases down to the original level.

Information on the EET time constants from measurements of the fluorescence decay curves in the whole spectral range between 500 – 700 nm can be gathered by analysing the decay-associated spectra (DAS).

Figure 16 shows the DAS of the QD-PBP hybrid complexes after excitation with 405 nm laser pulses at 295 K (left panel of Figure16) and 250 K (right panel of Figure 16). In both cases, a suitable fit of the data was achieved with three exponential components. The DAS of the measurements at 273 K is characterized by components with time constants of 140 ps (black curve), 640 ps (red curve) and 1.5 ns (blue curve) at room temperature. The spectrum of the 140 ps time constant exhibits a positive band at 530 nm and a pronounced negative peak in the region of 660 nm emission from the PBPs. This feature indicates that an EET from QDs to the PBP takes place with a time constant of 140 ps and that more than 90 % of the QDs are involved. Only small contributions with a fractional amount of less than 10 % and time constants longer than 140 ps are found in the green region. In the spectral region of the PBP luminescence around 660 nm, a pronounced rise kinetics (negative amplitude in DAS) is obtained with a time constant of 140 ps. In addition, a characteristic 1.5 ns decay of the PBP luminescence was resolved, which is typical for isolated PBP antenna rods, and an additional 640 ps component of comparable amplitude. This 640 ps component emerges most probably from conformationally distorted PBP complexes (see ref. (Schmitt et al., 2006)).

A markedly different DAS pattern was found at 250 K. A suitable fit of the data was achieved with three exponential components exhibiting time constants of 250 ps (black curve), 580 ps (red curve) and 2.5 ns (blue curve). The negative amplitude in the PBP emission (670 nm) is strongly reduced in comparison to the results obtained at 295 K, thus indicating that the EET from CdSe QDs to PBP is interrupted at temperatures below the freezing point of water. The pronounced amplitude of the 580 ps component (red curve) in the PBP emission (670 nm) indicates that a larger fraction of PBP antenna complexes is conformationally distorted in comparison to 295 K.

The results of the present study reveal that the CdSe QDs couple functionally via EET to the isolated PBP antenna complexes from *A. marina.* This coupling is reversibly distorted at temperatures below 273 K. It seems reasonable to assume that a conformational distortion due to the freezing process is responsible for the decoupling effect.

The coupling efficiency between CdSe/Zns-530-QDs and the PBP antenna of *A. marina* at room temperature was evaluated within the framework of Förster Resonance Energy Transfer (FRET). The

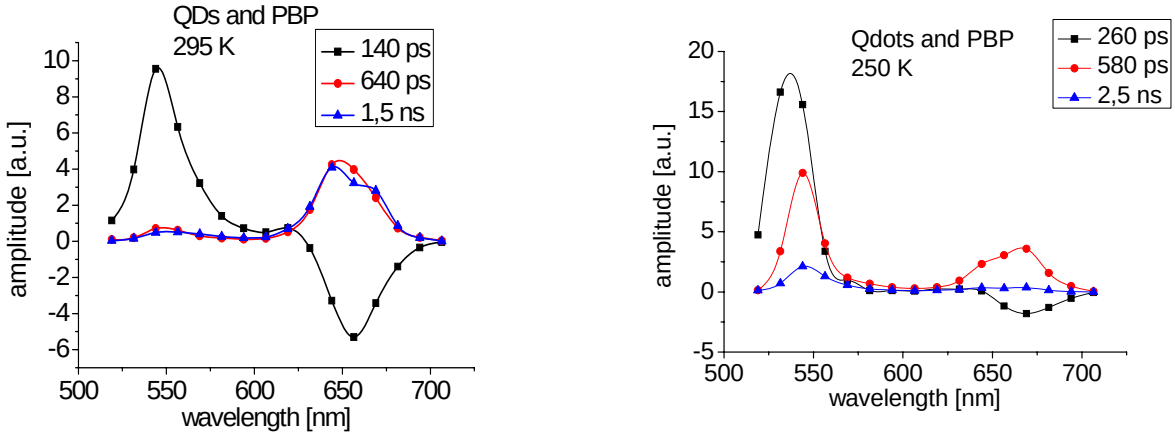

Figure 16. Decay-associated spectra of CdSe-530 QDs mixed with PBP from *A. marina* after excitation with 405 nm at room temperature (295 K, left side) and 250 K, right side. Data is redrawn from Schmitt et al. (2011).

efficiency η_{FRET} of this EET can be calculated by comparing the fluorescence intensity of the donor in the absence (I_D) and in the presence (I_{DA}) of the acceptor according to the formula $\eta_{FRET} = 1 - \frac{I_{DA}}{I_D}$.

After equilibration of the hybrid system of QDs and PBPs at room temperature, it was found that the fluorescence of the QDs decreases by about 75 %. A comparable result is obtained from a comparison of the average lifetime of the fluorescence decay curves of the QDs in the presence and absence of PBP. The average lifetime of the QDs in the absence of PBP ($\bar{\tau}_D$) was found to be about 1.1 ns at 530 nm. After addition of PBPs, this value decreased to $\bar{\tau}_{DA}$ = 230 ps. In this consideration, an average lifetime is taken into account instead of the multiphasic decay visible in the DAS (Figure 16). Therefore, the value for the efficiency η is not the efficiency of the coupled QDs, but an average efficiency that also takes into account the fraction of uncoupled QDs, which is estimated to be about 10 % according to the amplitude ratio of the different DAS components as shown in Figure16 (left panel). The total average leads to a value of $\eta_{FRET} = 1 - \frac{\bar{\tau}_{DA}}{\bar{\tau}_D} \approx 0.78$, which is in good agreement with the value of η_{FRET} = 0.75 as determined from the time-integrated fluorescence.

A more accurate evaluation of the DAS shown in Figure 16 (left panel) indicates that the lifetime $\bar{\tau}_{DA}$ = 140 ps reflects only the coupled QDs, i.e. that the EET in the coupled QDs is more efficient than suggested by the average value. The time-resolved results for the coupled fraction of QDs results in a value of $\eta_{FRET} = 1 - \frac{\bar{\tau}_{DA}}{\bar{\tau}_D} \approx 0.87$. Therefore, the DAS do not only show an average efficiency for FRET as found by time-integrated fluorescence measurements, but also allow to distinguish between the coupled and uncoupled species. Therefore, DAS provide a suitable tool for the selective evaluation of the efficiency of the coupled species.

From the measured time-integrated spectra of the PBP absorption and QD fluorescence, one can calculate the Förster radius R_0 for the QD-PBP hybrid system as given by eq. $R_0 = \left(A\Phi_F \frac{\kappa^2}{n^4} J(\lambda) \right)^{\frac{1}{6}}$.

Here, A is a constant, Φ_F denotes the quantum yield of the QDs which is about 0.3 according to (Medintz, Mattoussi, 2009). κ^2 denotes the orientation factor which is $\kappa^2 \approx 2/3$ for randomly organized QD/PBP hybrid complexes.

The real part of the complex refraction index of the surrounding medium is given by $n \approx 1.33$ for aqueous buffer solution.

$J := \frac{\int_0^\infty F_D(\lambda)\varepsilon(\lambda)\lambda^4 d\lambda}{\int_0^\infty F_D(\lambda) d\lambda}$ determines the normalized overlap integral between the normalized donor fluorescence $F_D(\lambda)$ and the acceptor extinction $\varepsilon(\lambda)$. For the QD/PBP hybrid system presented in this study a value of $J = 1{,}23 \cdot 10^{15} \frac{nm^4}{Mol \cdot cm}$ is obtained and the Förster radius is calculated to be $R_0 \approx 4.4\,nm$.

From the time-resolved spectra, the value of η_{FRET}= 0.87 was found for the QDs coupled to PBP and therefore the average distance between the center of a QD and the next neighbouring chromophore of PBP can be calculated as follows:

$R_{12} = \left(\frac{1-\eta_{FRET}}{\eta_{FRET}} \right)^{\frac{1}{6}} R_0 \approx 3.2\,nm$ and the rate constant fro FRET $k_{FRET}(R_{12}) = \frac{1}{\bar{\tau}_D} \left(\frac{R_0}{R_{12}} \right)^6 \approx (140\,ps)^{-1}$.

These findings are schematically summarized in

Figure17 including earlier data on the EET inside the PBP as shown in Figure 11.

Figure 17 presents a schematic view of the CdSe/ZnS-QDs bound electrostatically to the PBP antenna of *A. marina*. The CdSe QDs with fluorescence emission at 530 nm transfer the excitation energy to the PBP antenna within 140 ps (red arrow). Other studies revealed time constants up to 240 ps, which would correspond to a distance of 3.5 nm between the QDs and the primary acceptor pigment in the PBP antenna. Former studies showed that the equilibration along the PBP antenna (PC/APC molecules) occurs within <20 ps (see Figure 11). The luminescence of the PBP antenna is characterized by maxima at 650 nm (PC) and 665 nm (APC).

Investigation of the FRET efficiency between CdSe/ZnS nanocrystals and PBP complexes revealed that the temperature-dependent value of the spectral overlap integral *J* can be described by a Boltzmann distribution at low temperatures, but in

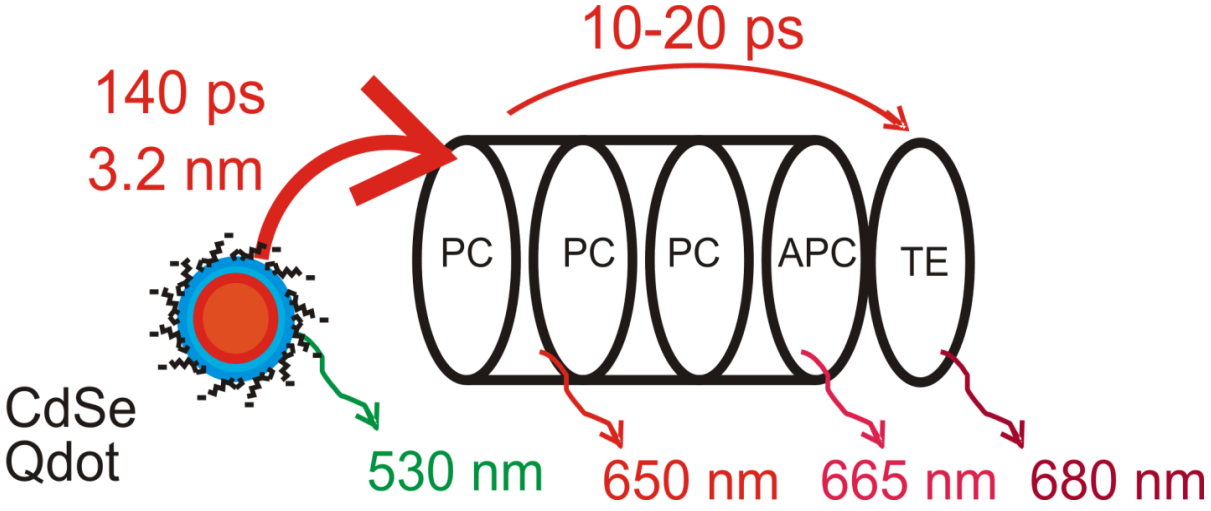

Figure 17. left side: schematic view of the CdSe/ZnS-QDs bound electrostatically to the PBP antenna of *A. marina* as published in Schmitt, 2011; Schmitt et al., 2011. The CdSe-530 QDs exhibit fluorescence emission at 530 nm and transfer the excitation energy to the PBP antenna within 140 ps (red arrow) at room temperature. The luminescence of the PBP antenna occurs with maxima at 650 nm (PC) and 665 nm (APC).

addition marked conformational changes must occur around 0°C (see ref. (Schmitt, 2010)). This transition leads to an interruption of the EET at low temperatures that can not be explained by spectral narrowing, which typically occurs in the low temperature regime. Further details of these findings are described in refs. (Schmitt, 2010, 2011; Schmitt et al., 2011, 2012).

Hybrid systems consisting of artificial nanostructures and complexes of biological origin offer a wide variety of applications in photovoltaics, optoelectronics, sensorics, molecular imaging and medical applications. Complexes isolated from the photosynthetic apparatus provide functionally optimized nanoscale devices for the construction of light-driven operational units.

4. Studies on fluorescent proteins (FPs)

Fluorescent proteins are key tools in modern life sciences. Especially their application in fluorescence microscopy revealed functional properties of single molecules and their distribution inside the cell. This revolutionized our view on biological systems by revealing spatial distribution and dynamics of cell compartments and single molecules on the nanometer scale. Today,

fluorescent proteins are available with various properties, various colors, switching properties, pH sensitivity or sensitivity to various other chemical compounds (see (Shaner et al., 2005; Stepanenko et al., 2011) and references therein).

One main feature of the fluorescent proteins based on GFP is the possibility of genetic encoding in order to express them simultaneously or in fusion with a certain protein of interest. Thus, the fluorescent protein can be fused as an optical "tag" to a certain protein.

We demonstrate how structural parameters of an eGFP-tagRFP fusion protein (termed "FRET construct" herein) formed by eGFP and tagRFP linked via a 5 amino acid-long linker can be analyzed by combining fluorescence emission spectroscopy, 2-dimensional excitation/emission spectroscopy, time resolved ps-emission spectroscopy and fluorescence correlation spectroscopy (FCS). The pentapeptide connects the two single, barrel-shaped fluorescent proteins in the FRET-construct that therefore contains a flexible connection between the two FP moieties.

Figure 18 shows green fluorescent protein bound to proteins which are localized in the plasma membrane while cytosolic proteins are marked with red fluorescent protein (RFP).

4.1. Distance determination of the chromophores of eGFP and tagRFP in eGFP-tagRFP fusion protein by FRET

The determination of structural parameters via indirect effects like amplitude or lifetime changes in fluorescent proteins requires a strict comparison of the observed fluorescence of the investigated structure with reference samples. Labelled cells should always be carefully compared with the cells that do not express the fluorescence marker to quantify the influence of autofluorescence. In addition, cross-talk between the spectral donor and acceptor channels used, direct acceptor excitation or incomplete EET make an accurate determination of the FRET efficiency from purely amplitude-based fluorescence measurements a difficult task that needs complex controls and corrections (Gordon et al., 1998). We show how combined spectral fluorescence techniques including time-

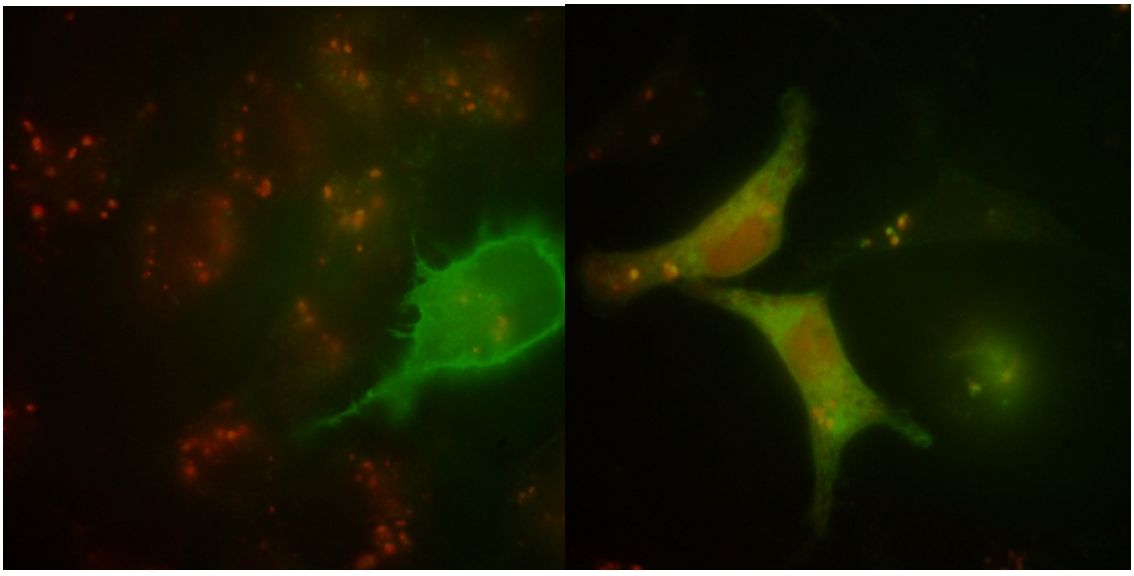

Figure 18. Shows transfected cells of the chinese hamster ovary (CHO-K1) were membrane bound ion channels are marked with GFP while cytoplasmatic proteins are marked with RFP.

integrated fluorimetry and PLE and additional time-resolved studies (TWCSPC and FLIM) allow a more accurate determination and the identification of coupled and uncoupled subensembles.

For the determination of the donor-acceptor distance in the eGFP-tagRFP fusion protein (FRET contruct), we first started to investigate cells expressing a mutated version of this FRET construct, which is not able to transfer excitation energy from eGFP to tagRFP, since the tagRFP carries the G65S mutant that is not able to form the red chromophore. Therefore, this eGFP-tagRFP fusion protein with G65S mutation (FRET(-) - construct) is not able to exhibit FRET.

Cells expressing the FRET(-) construct monitored in the wavelength regime at 525 nm (emission filter 525/35, left side of Figure 19) and 600 nm (emission filter 605/40, right side of Figure 19) after excitation with 470 nm are shown in Figure 19.

The whole emission spectrum of the FRET (-) construct after excitation with 405 nm is shown in Figure 20.

The emission of the FRET(-) construct as shown in Figure 20 resembles the spectrum of GFP. Small deviations most likely result from autofluorescence of the CHO-K1 cells. The spectrum is typically characterized by the main emission peak at 510 nm and an additional broad shoulder at 540 nm.

To analyse the excited state dynamics in the FRET(-)-expressing cells, a novel position-sensitive single photon-counting detector (quadrant anode, QA , IfN Magdeburg) based on microchannel plate photomultipliers and a segmented anode that allows the calculation of spatial coordinates of the impinging electron avalanche from the charge distribution on 5 separated anodes was used (for the detection principle and the microscopic setup see chap. 2.3 and (Vitali, 2011). The detector allows the pixel-wise analysis of the fluorescence dynamics. For that purpose, a huge amount of photons ($\sim 10^6$ s^{-1}) has to be collected in short measurement times to ensure sample stability during the measurement. IfN Magdeburg therefore refined the QA technology with the implementation of a Proximity-MCP-PMT measurement head.

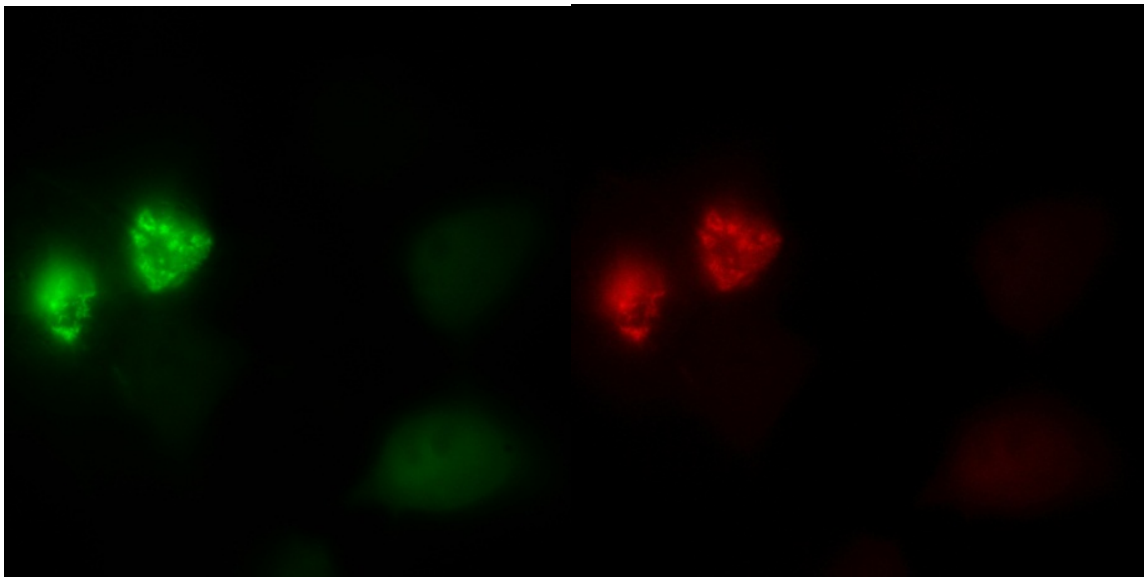

Figure19. CHO-K1 cells expressing eGFP-tagRFP(G65S) (FRET(-) construct) after excitation with 470 nm observed in the “green channel” (left side, em-filter 520/35) and in the “red channel” (right side, em-filter 605/40).

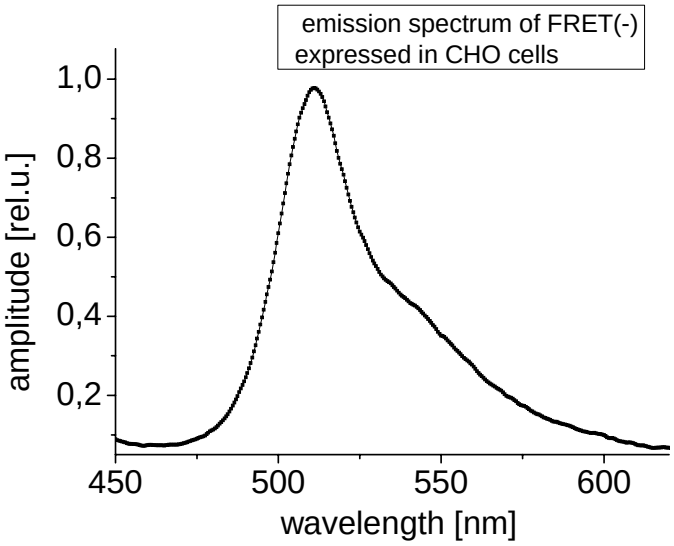

Figure 20. Fluorescence spectrum of the FRET(-) protein, expressed in CHO-K1 cells after excitation with 405 nm.

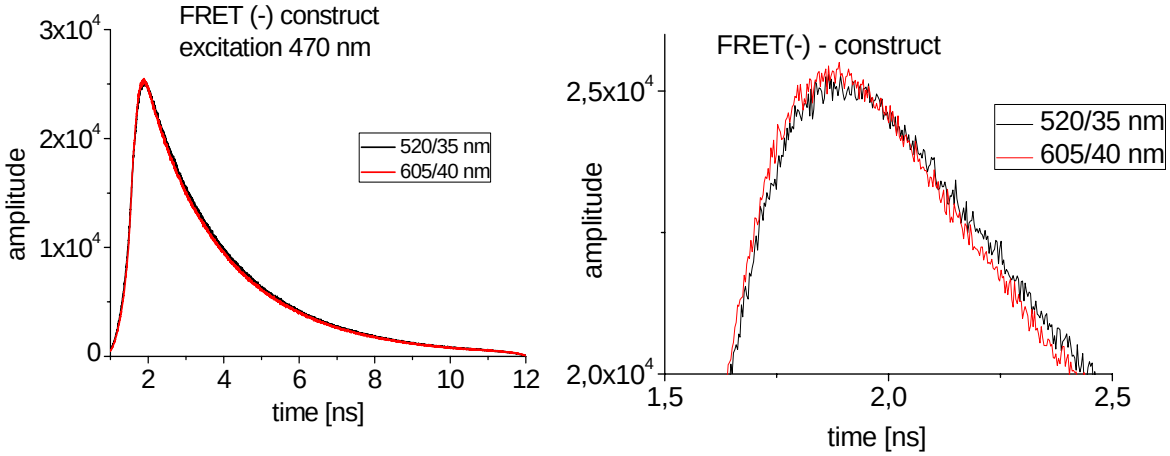

Figure 21. Fluorescence dynamics of the cells shown in Figure in the "green channel" (520/35 nm), marked in black in comparison to the "red channel" (605/40 nm) after excitation with 470 nm laser light and after normalization. Data is measured with the QA-Proximity-MCP-PMT-measurement head (IfN, Magdeburg). The fluorescence decay is plotted linear (left side) with an amplification of the temporal maximum of both normalized curves in logarithmic scale (right side).

The time courses of the eGFP visible in the "green channel" and "red channel" as shown in Figure 19 after excitation with 470 nm pulsed laser light is shown in Figure 21 for the green channel (black curves) and red channel (red curves). The full decay is depicted in Figure 21, left side, while Figure 21, right side exhibits an amplification of the temporal emission maximum.

Both curves match clearly with only very small deviation between the green and the red channel that is close to the resolution limit. This similarity

of the fluorescence decay in the emission regime of eGFP (520/35 nm) and the emission regime of tagRFP (605/40 nm) clearly indicates that EET does not occur in the FRET (-) construct.

2-dimensional PLE spectroscopy nicely visualizes EET processes as "off diagonal" elements in the PLE plot (see chap 2.2. and ref. (Schoeps, 2009).

Figure 22 shows PLE plots of pure (isolated) eGFP and tagRFP. The fluorescence is localized on the "diagonal" of equal excitation and emission wavelength slightly shifted towards longer wavelengths due to the Stokes shift. Such behavior is typical for isolated chromophores. If donor pigments can excite acceptor states to fluorescence via an EET process, one expects a long wavelength emission after excitation of the donor as characteristic "off diagonal elements" in the lower right corner of the PLE plot.

After characterization of the FRET(-) construct, CHO-K1 cells were transfected with the eGFP-tagRFP fusion protein (FRET construct) to analyze the EET efficiency by accurate comparison with the FRET(-) construct.

The CHO-K1 cells expressing the FRET construct and monitored in the wavelength regimes at 525 nm (emission filter 525/35, left side of Figure 23) and 600 nm (emission filter 605/40, right side of Figure) after excitation with 470 nm are shown in Figure 23.

Figure 24 shows the emission spectrum of the FRET construct after excitation with 405 nm.

In marked contrast to Figure 20, the spectrum shown in Figure 24 exhibits a second peak around 580 nm, which is not observed with eGFP expressed alone or in the FRET(-) construct. The 580 nm shoulder is typical for the tagRFP luminescence (see PLE plot of tagRFP in Figure 22, right side). This pronounced shoulder is already a strong indication for an EET from eGFP to tagRFP. Considering the spectrum of the FRET(-) construct (Figure 20) or the PLE plot of eGFP expressed alone (Figure 22, left side), one can imagine the difficulty in determining the FRET efficiency from such spectra as GFP only exhibits long wavelength emission also at 580 nm. In addition, the fluorescence spectra were obtained after excitation with a 405 nm laser, which might excite

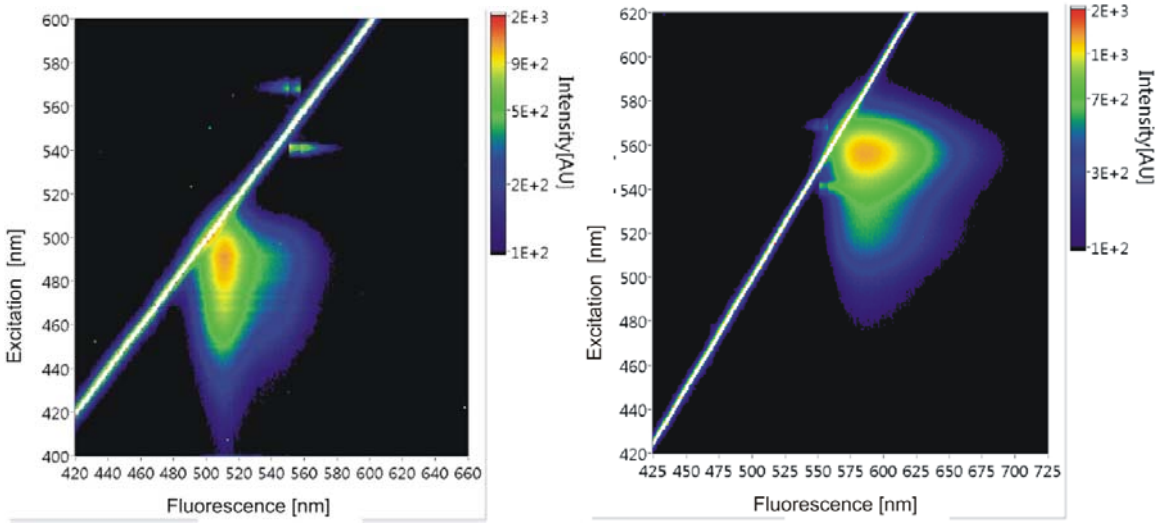

Figure 22. PLE plot of GFP in the wavelength regime between 400 nm and 600 nm (excitation) and 420 nm and 660 nm (emission) (left side) and RFP in the wavelength regime between 420 nm and 620 nm (excitation) and 425 nm and 725 nm (emission). The color represents the intensity of the observed emission (x-axis) in dependence on the excitation wavelength (y-axis).

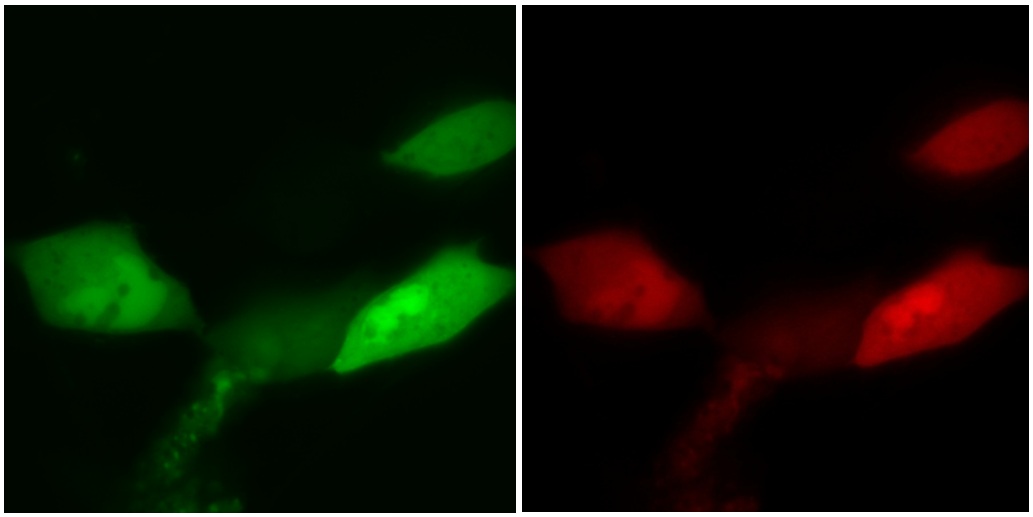

Figure 23. CHO-K1 cells marked with eGFP-TagRFP fusion protein (FRET construct) after excitation with 470 nm observed in the "green channel" (left side, em-filter 520/35) and in the "red channel" (right side, em-filter 605/40).

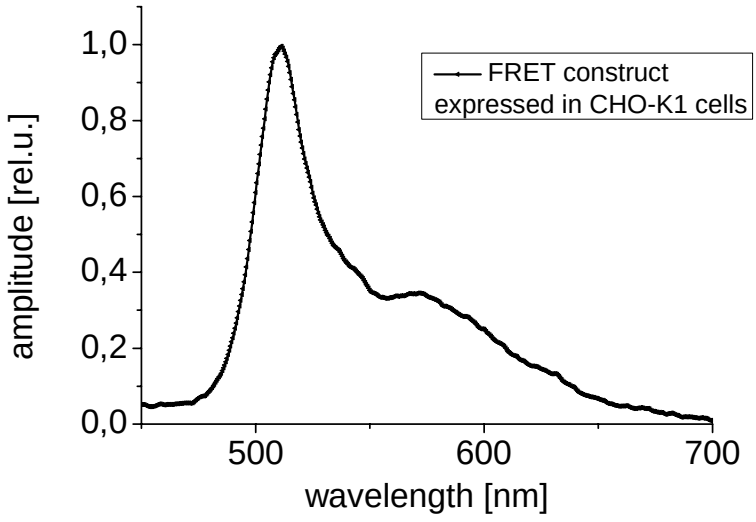

Figure 24. Fluorescence spectrum of the FRET construct containing eGFP and tagRFP with functional chromophore expressed in CHO-K1 cells, after excitation with 405 nm.

both, donor and acceptor simultaneously. To analyse the wavelength dependency of the donor-acceptor (i.e. GFP-tagRFP) coupling, PLE plots of the FRET construct were registered, as shown in Figure 25.

Figure 25 shows the response of the eGFP-TagRFP FRET construct in CHO-K1 cells after excitation in the whole spectral range between 400 nm and 700 nm. Next to the diagonal of the excitation light, the emission of eGFP is clearly visible at 510 nm with an excitation maximum at 490 nm and tagRFP is most prominent at 580 nm after excitation at 560 nm. The energy which is transferred to the acceptor via FRET is visible as an "off diagonal" element with an emission maximum at 580 nm (tagRFP

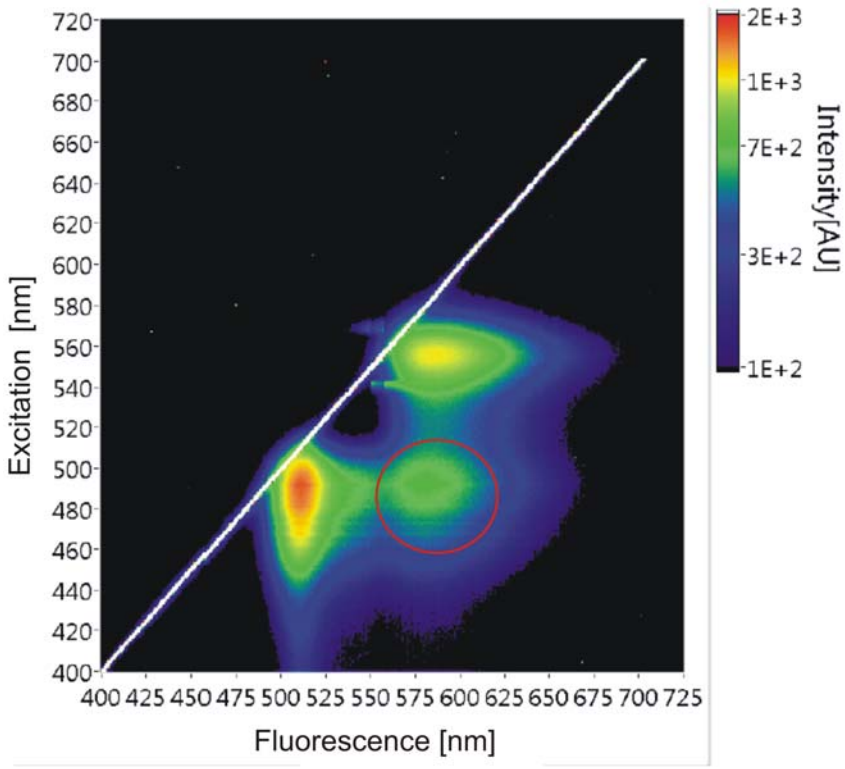

Figure 25. PLE plot of the eGFP-tagRFP FRET construct in the wavelength regime between 400 nm and 720 nm (excitation) and 400 nm and 725 nm (emission) . The color represents the intensity of the observed emission (x-axis) in dependence on the excitation wavelength (y-axis).

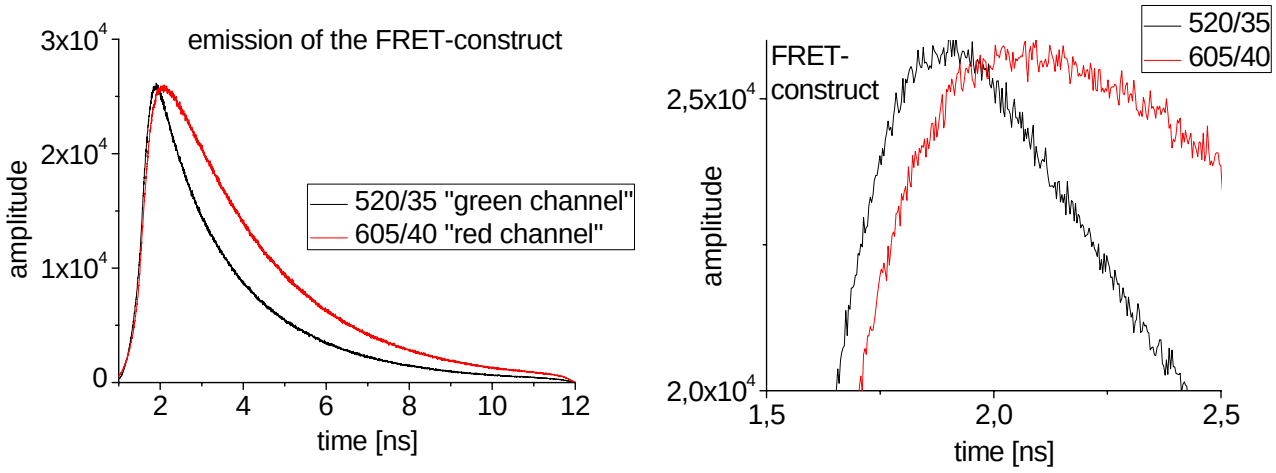

Figure 26. Fluorescence dynamics of the cells shown in Figure in the “green channel” (520/35 nm), marked in black in comparison to the “red channel” (605/40 nm) after excitation with 470 nm laser light and normalization. Data was measured with the QA-Proximity-MCP-PMT head (IfN, Magdeburg). The fluorescence decay is plotted on a linear scale (left side), and in higher magnification of both normalized curves on a logarithmic scale (right side).

emission) after excitation at 490 nm (eGFP absorption maximum). In Figure 25, the emission maximum is marked with a red circle.

The time courses of the eGFP fluorescence decay in the "green channel" and "red channel" as shown in Figure 23 after excitation with 470 nm pulsed laser light is shown in Figure 26 for the green (black curves) and red channel (red curves). The full decay is depicted in Figure 26, left side, while Figure 26, right side, depicts the emission maximum on an expanded time scale.

In marked contrast to Figure 21, the two curves in Figure 26 differ strongly. The emission in the red channel (605/40) is enhanced and appears shifted towards longer times.

Figure 26 shows that a pronounced "rise kinetics" can be discriminated, which should lead to a negative amplitude in the decay-associated spectra (DAS) at 605 nm compared to 520 nm. The fluorescence in the red channel (605/40 filter) rises in time with a clear shift of the maximum by about 200 ps compared to that of the green fluorescence (520/35 filter). The temporal maximum of the red emission is reached with temporal shift compared to the green emission (see Figure 26, right side).

For a quantitative analysis of the excited state dynamics, the fluorescence decay of the FRET construct was monitored in the whole spectral range between 500 nm and 650 nm after excitation with 470 nm pulsed laser light. The results are plotted as decay-associated spectra (DAS) in Figure 27.

The DAS in Figure 27 show that the fluorescence decay of the eGFP-tagRFP fusion protein exhibits three exponential components. The eGFP fluorescence (510 nm) mainly decays with time constants of 2.2 ns (black squares) and 800 ps (blue triangles), but a small fraction of about 20 % exhibits a fluorescence decay component with a time constant of 250 ps (red circles). This component shows a clear "rise kinetics", i.e. a negative fit component in the emission regime of RFP at 580 nm. The RFP mainly decays with 2.2 ns (black curve).

From this data, one can conclude that only a small fraction of the eGFP molecules transfers energy to their tagRFP fusion partner. This fraction is estimated to about 20 % of all FRET construct molecules.

Within the coupled FRET pairs that exhibit efficient energy transfer, the EET is rather fast with a time constant for the energy transfer of 250 ps.

This precise discrimination between coupled and uncoupled FRET pairs (20 % to 80 %) and the additional time constants for EET of 250 ps is not visible from the fluorescence data shown in Figure 24 and Figure 25.

The prominent formula $\eta_{FRET} = 1 - \frac{I_{DA}}{I_D}$ which was also used to determine the effective average energy transfer from quantum dots to the PBP antenna of *A. marina* (chapter 2.3) would lead to a misleading interpretation, since it would suggest an average EET, which is a true value for the average ensemble, but neglects the fact that a small fraction of the eGFP-tagRFP pairs are strongly coupled while the bigger part (80 %) of the FRET construct molecules do not reveal EET at all.

The pure evaluation of the amplitudes of the emission intensity of donor molecules in the presence of acceptors I_{DA} and the donor molecules in the absence of acceptors I_D to determine the FRET efficiency $\eta_{FRET} = 1 - \frac{I_{DA}}{I_D}$ is especially wrong, if energy transfer is possible in both directions, from the donor to the acceptor and also backwards from the acceptor to the donor. Such problems and the necessary corrections of the Förster formula are analysed in detail in ref. (Schmitt, 2011).

The time-resolved analysis and determination of DAS is by far more accurate for the selective determination of the FRET efficiency, no matter

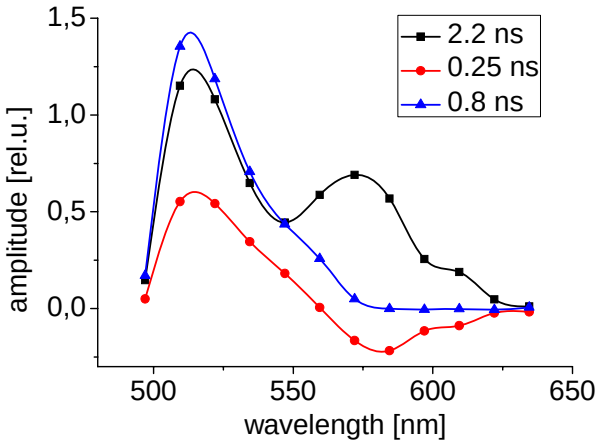

Figure 27. Measured DAS of the eGFP-tagRFP fusion protein (FRET construct) after excitation with 470 nm. The fluorescence decay exhibits three exponential components with time constants of 250 ps (red curve), 800 ps (blue curve) and 2.2 ns (black curve).

whether strongly coupled, weakly coupled and totally uncoupled donor-acceptor pairs are present. At first, the Förster radius R_0 is determined from the spectral properties of donor and acceptor as outlined in chapter 2.3: $R_0 = \left(A\Phi_F \frac{\kappa^2}{n^4} J(\lambda) \right)^{\frac{1}{6}}$ where A is a constant, Φ_F denotes the quantum yield of the QDs which is about 0.3 according to (Medintz, Matoussi, 2009). κ^2 denotes the orientation factor. The real part of the complex refraction index of the surrounding medium is denoted as n.

$J := \frac{\int_0^\infty F_D(\lambda)\varepsilon(\lambda)\lambda^4 d\lambda}{\int_0^\infty F_D(\lambda) d\lambda}$ determines the normalized overlap integral between the normalized donor fluorescence $F_D(\lambda)$ and the acceptor extinction $\varepsilon(\lambda)$. From this data, the rate constant for the energy transfer is calculated according to $k_T = \frac{1}{\tau_D}\left(\frac{R_0}{r}\right)^6$ where r denotes the distance of the balance points of donor (GFP) and acceptor (TagRFP) and τ_D symbolizes the fluorescence lifetime of the isolated donor.

For the determination of R_0 of the eGFP-tagRFP FRET construct, a quantum efficiency of the donor was assumed as $\Phi_F = 0.6$, the refraction index n was assumed to be 1.3 ± 10 % and κ^2 was set to 2/3 ± 50%. The extinction spectrum of tagRFP after expression in CHO-K1 cells could not be measured and was therefore taken from literature. Finally, the spectral overlap integral was calculated to 1.45 · 10^{15} nm^4/(Mol*cm) ± 0.15 · 10^{15} nm^4/(Mol*cm) and the Förster radius was determined to R_0 = 4.7 nm ± 0.6nm.

The excited state lifetime τ_D of eGFP was measured to 2.7 ns, including the value k_T = 280 ps the distance of the transition dipole moments of eGFP as donor and tagRFP as acceptor in the FRET construct was calculated to r = 3.2 nm ± 0.6 nm.

4.2. Hydrodynamic radius of eGFP and eGFP-tagRFP determined by fluorescence correlation spectroscopy (FCS)

The FRET quantification techniques provide a very precise nanometer-scale ruler to measure intramolecular distances at sub-nanometer accuracy. The main reason for this accuracy is the dependence of the Förster energy transfer

efficiency on the 6th power of the distance between donor and acceptor dipole.

Fluorescence correlation spectroscopy (FCS) is suitable to determine the hydrodynamic radius of single molecules and protein chromophores by taking the G(τ) autocorrelation function and calculating the average diffusion time of single molecules across the diffraction-limited focus of a laser (the so-called "confocal volume").

The simultaneous performance of FCS and fluorescence lifetime measurements allows the determination of intramolecular distances between donor and acceptor states (FRET) and, additionally, the overall size of the macromolecules in terms of a hydrodynamic radius.

The FCS curves ($G(\tau)$) are autocorrelation signals that are determined from single molecules that diffuse through the focused laser above a microscope objective with high numerical aperture. Generally, for the determination of $G(\tau)$ the fluorescence signal $\langle F(t)\rangle$ is compared to a somewhat later fluorescence signal $\langle F(t+\tau)\rangle$ according to: $G(\tau)=\frac{\langle F(t+\tau)F(t)\rangle}{\langle F(t)\rangle\langle F(t)\rangle}$ (Lakowicz, 2006) For the 2-dimensional situation of a single molecule diffusing through a planar two-dimensional Gaussian laser spot, it can be shown that this signal is equal to $G(\tau)=\frac{1}{\langle N\rangle}\cdot\frac{1}{\left(1+\tau/\tau_D\right)}$ where $\langle N\rangle$ denotes the expectation value of molecules found in the laser $G(\tau)=\frac{1}{\langle N\rangle}\cdot\frac{1}{\left(1+\tau/\tau_D\right)}$ where $\langle N\rangle$ denotes the expectation value of molecules found in the laser focus as time average and τ_D determines the „diffusion time", i.e. the characteristic time the molecule on average is found in the laser focus (Lakowicz, 2006).

With this formula, one can fit the FCS data with only two parameters. These parameters

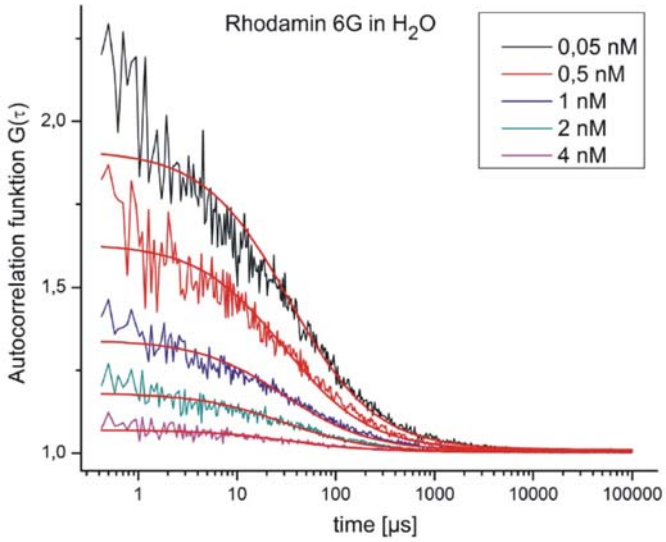

Figure 28. Fluorescence correlation curves of Rhodamine 6G at various concentrations between 4 nM (magenta curve) and 0.05 nM (black curve). The red line shows a data fit according to the 2-dimensional autocorrelation function $G(\tau)=1/\langle N\rangle\cdot 1/(1+\tau/\tau_D)$

are widely independent from each other, since $\langle N \rangle$ finally denotes the value $(G(0))^{-1}$ and τ_D is found at the point of inflection of the two-dimensional autocorrelation function $G(\tau) = \frac{1}{\langle N \rangle} \cdot \frac{1}{\left(1 + \tau / \tau_D\right)}$.

Typical FCS traces as measured for Rhodamine 6G in aqueous solutions are shown in Figure 28 for various concentrations between 0.05 nM and 4 nM.

The red straight lines in Figure 28 denote fits to the data according to the two-dimensional autocorrelation function. From these fits, τ_D for Rhodamine 6G was calculated to 30 ± 3 µs, in good agreement with (Selanger et al., 1977).

With $s^2 = x^2 + y^2$ for the extension x and y of the two-dimensional Gaussian laser beam, the diffussion constant D, the viscosity of the medium η, the temperature T and the Boltzmann constant k_B the hydrodynamic radius R_{hyd} can be calculated as $R_{hyd} = \frac{k_B T}{6\pi\eta D}$ with $\tau_D = \frac{s^2}{4D}$. Further extensions of the theory allow the inclusion of a three-dimensional FCS volume, triplet formation and further deviations from the ideal case (Rigler, Mets, 1992; Rigler et al., 1993; Eggeling et al., 1998). For the Rhodamine 6G molecule, a hydrodynamic radius R_{hyd} (Rhodamin) = 0.3 nm is determined.

To calculate the hydrodynamic radius for eGFP and the eGFP-tagRFP FRET construct, FCS curves for both proteins in aqueous solution were measured and analyzed as shown in Figure 29.

From the data of eGFP shown in Figure 29, left side, and the resulting diffusion time of 100 µs, the hydrodynamic radius was calculated to 3.3 nm. This value is in good agreement with the known dimensions of the GFP barrel, which is about 2 nm in diameter and up to 4 nm in length.

Interestingly, the eGFP-tagRFP FRET construct appears much bigger with a hydrodynamic radius of 12.6 nm calculated from the measured diffusion time of τ_D = 470 µs (see Figure 29, right side). Figure 30 summarized the view onto the eGFP-tagRFP FRET construct.

While the hydrodynamic radius of eGFP calculated to 3.2 nm is in good agreement with the expectations, the hydrodynamic radius of the FRET construct consisting of the eGFP-tagRFP fusion protein was 12.6 nm, which is by a factor of about four times larger than the calculated distance between the transition dipole moments of the donor (eGFP) and the acceptor (tagRFP) according to FRET (see chapter 4.1).

The profound deviation might be explained by a more complex geometrical structure of the molecule that is hampered in diffusion possibly due to the flexibility of the connecting peptide linker. Another possibility explaining the much larger hydrodynamic radius than expected from a monomeric FRET-construct might be the formation of higher oligomers. On the other hand, the suitable fit of the FCS curve of the FRET-construct (Figure 29, right side) rules out that the sample is represented by a broad distribution of various higher oligomers with strongly varying size.

The simple theory presented here is suitable to determine the hydrodynamic radius of a diffusing sphere. The measured deviations indicate that the protein can not be described well by a sphere, but that it exhibits an intrinsic substructure.

Our studies on the eGFP-tagRFP FRET construct exemplify how the combined analysis of FRET and FCS reveals two structural parameters: i) The distance of the dipole moments in the eGFP-tagRFP construct of 3.2 nm, and ii) the hydrodynamic radius of the FRET construct of 12.6 nm, which indicates that the FRET construct might form higher oligomers, or is otherwise hampered in diffusion and, therefore, not well described by the hydrodynamic radius as a single parameter that reduces the diffusing structure in FCS to a sphere.

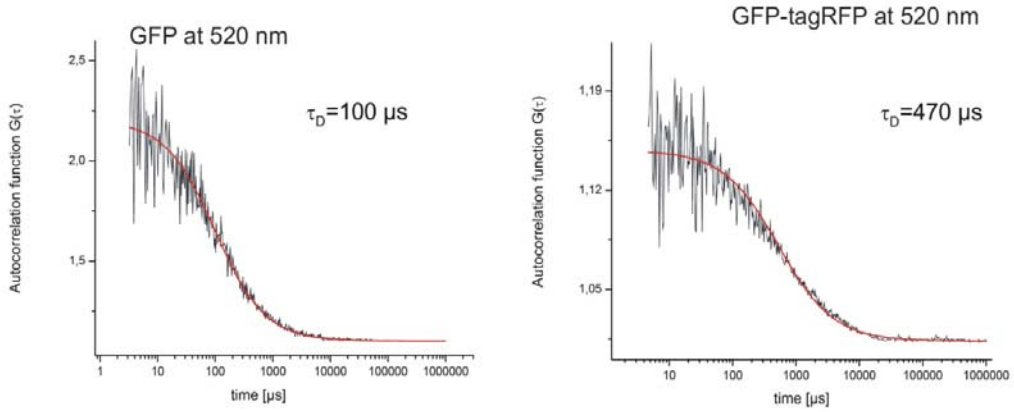

Figure 29. Fluorescence correlation curve of eGFP at a concentration of 0.5 nM (left side) measured at 520 nm after excitation with 470 nm and fluorescence correlation curve of the eGFP-tagRFP FRET construct at a concentration of 0.5 nM (right side) measured at 520 nm after excitation with 470 nm. The red line shows a fit to the data according to the 2-dimensional autocorrelation function $G(\tau)=1/\langle N\rangle \cdot 1/(1+\tau/\tau_D)$

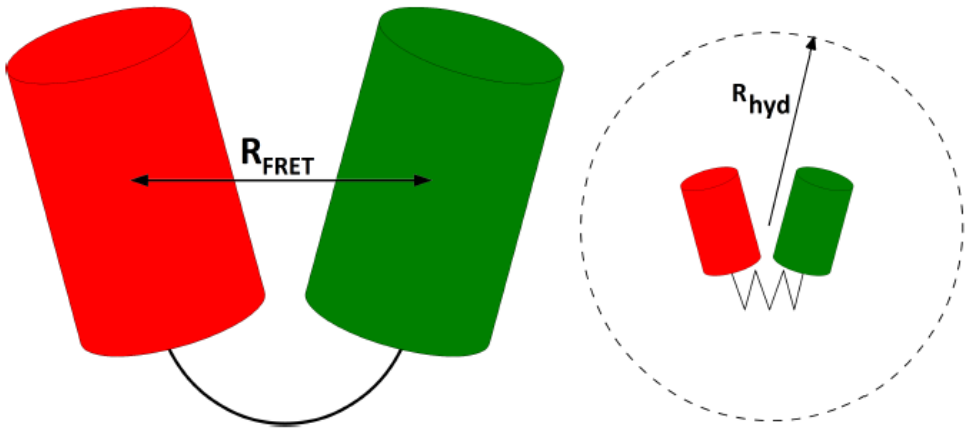

Figure 30. Schematic view of the eGFP-tagRFP FRET construct with a typical dipole distance between the donor and the emitter of 3.2 nm (R_{FRET}, left side), while a much larger hydrodynamic radius of 12.6 nm was determined (right side).

The results gained on eGFP only (R_{hyd} = 3.3 nm) are in good agreement with the expectations from crystal structures.

5. Summary

In summary, the combination of complementary techniques for the study of biological samples is suitable to refine the results obtained from single, isolated techniques. At first, EET processes can better be related to structural parameters by combined FRET studies based on fluorescence amplitudes and time-resolved spectroscopy. Second, EET processes that cover a wide range from the fs up to the ns time scale are unraveled by combining fs pump-probe spectroscopy with time

resolved fluorescence studies. The addition of FCS helps to cover the subsequent long time ranges and provide additional parameters that are related to the diffusion of the sample (the overall apparent hydrodynamic radius of FRET constructs in contrast to the intrinsic donor-acceptor distance). Temperature-controlled studies show how the sample organization changes due to freezing of the environmental matrix. As EET and energetic modulation by the environment (site energy modulations) appear on a large range of time scales from fs to µs and additionally lead to similar effects for selected spectroscopic technique, special site-selective methods and an accurate theoretical analysis have to be performed in parallel in order to separate the pigment-protein interaction from the pigment-pigment interaction.

These are some selected outcomes gained by the combined techniques as outlined in this review. In detail, the experimental results showed that ultrafast energy equilibration occurs in the phycobiliprotein (PBP) antenna of *A. marina* between different phycocyanine (PC) molecules (< 1 ps), which are bound to a hexameric protein structure followed by the equilibration between the phycocyanine and the allophycocyanine (APC) containing hexamers with a time constant of 3-5 ps (Theiss, 2006; Theiss et al., 2008, 2011). A subsequent relaxation of the excitation energy from PC and APC containing hexamers of the membrane extrinsic PBP antenna to spectrally red-shifted APC molecules, which are most probably located in the linker protein, was resolved to 20 (± 10) ps . In whole *A. marina* cells, the energy transfer between the PBP antenna and the Chl *d* containing membrane-intrinsic antenna complex was found to occur within an additional 50 (± 5) ps transfer step. Therefore, the excitons reach the reaction centre inside the membrane intrinsic Chl *d* complexes within 70 ps in *A. marina*. This value is three times faster than typically found in cyanobacteria containing bigger PBP and Chl *a* containing antenna complexes. The distance of the terminal emitter of the PBP antenna in *A. marina* and the nearest Chl *d* molecule was determined to 3.3 (± 0.3) nm according to the theory of Förster resonance energy transfer. This distance changes at 0°C leading to a decoupling of the PBP antenna from the membrane intrinsic Chl *d* antenna. The mechanism could help to construct intelligently switchable light-harvesting systems. The fast exciton diffusion due to the tiny one-dimensional structure has the disadvantage of a lower light absorption cross section, which is about four times smaller in *A. marina* compared to other cyanobacteria.

In WSCP, which exhibits an unusually high photostability of its bound chlorophyll dimers, a combined influence of pigment-pigment and pigment-protein dynamics determines the time-resolved fluorescence spectra. The fluorescence dynamics of WSCP occurs with three time constants at deep temperatures (10 K). From the data of femtosecond absorption spectroscopy, the distance of the two coupled Chl molecules in WSCP could be determined to 0.74 nm. Both chlorophyll molecules were assumed to form an "open sandwich" configuration, which was later confirmed by X-ray crystallography. Additional site-selective hole burning studies revealed that two distinguishable protein configurations exist that modulate the site energies of the bound Chl molecules. Most of the experimental data obtained on WSCP could be consistently described assuming a strongly bound Chl dimer that is modulated by the protein environment. In that way, the ultrafast kinetics is described as excitonic relaxation, and the long ns fluorescence decay, which is strongly temperature dependent, was explained by a relaxation of the coupled Chl dimer. Intermediate time constants measured as 100 ps in the fluorescence dynamics, which were not easy to explain by the pigment-pigment interaction, could be successfully related to the pigment-protein interaction.

In hybrid complexes consisting of CdSe/ZnS quantum dots (QDs) and PBP antenna complexes from *A. marina* that undergo self-assembly in aqueous solution, strong EET was observed from the QDs to the PBP complexes. This EET was interrupted at temperatures below the freezing point of the buffer solution. After subsequent rewarming,

a fast re-establishment of the coupling was observed. Time-resolved fluorescence studies showed that the most strongly bound QDs transfer more than 90 % of the excitation energy to the acceptors (PBP) with a time constant of 140 ps. With the theory of Förster Resonance Energy Transfer (FRET), the distance between the transition dipole moment in QDs and the next neighboring phycocyanobilin was calculated to 3.2 nm.

Fluorescence correlation spectroscopy (FCS) is suitable to determine the hydrodynamic radius of single molecules and protein chromophores by evaluating the G(τ) autocorrelation function and calculating the diffusion time. FCS and fluorescence lifetime measurements were done simultaneously with a novel Fluorescence Lifetime Imaging Microscopy setup (FLIM) with an integrated Single-Photon-Avalanche-Diode (SPAD). We determined the hydrodynamic radius of eGFP to 3.3 nm. A FRET construct consisting of the eGFP-tagRFP fusion protein was observed with a much larger hydrodynamic radius of 12.6 nm, which might be explained by a more complex geometrical structure of the molecule that has more degrees of freedom or by the formation of higher oligomers.

In addition to FCS, the setup allows the determination of the fluorescence lifetimes and, therefore, the calculation of the center-to-center distance of the molecular transition dipoles in eGFP and tagRFP, which was determined to 3.2 nm according to the theory of Förster Resonance Energy Transfer.

6. Conclusion and outlook

It must be the clear goal of each experimenter to extract all accessible information from an investigated sample. A selective look is suitable to answer a certain question related to the experiment but a thorough description needs combined complementary techniques and multiparameter imaging.
By utilization of combined spectroscopic methods employing ultrafast absorption pump-probe experiments with fs laser flashes, ps fluorescence decay curves that are determined in the range of several ps up to 100 ns and fluorescence correlation spectroscopy that can determine the G(τ) function in a wide range between sub µs up to several hours, one can cover more 20 orders of magnitude in the time domain regarding the observation of fluorescence samples.

Long-term fluorescence microscopy observing cell migration and growth for days and additional techniques that measure plant growth and changes in the biosphere could even extend this time scale. Therefore, the hierarchically organized structures of plants growing over more than 12 orders of magnitude in space ranging from the pm-dimension of electronic orbitals up to tens of meters sized plants (see Figure 1 and Figure 2) and the dynamics that shows an even wider range of up to 26 orders of magnitude in time ranging from the fs dynamics of light absorption to the life time of trees and certain see plants up to thousands of years can be nearly fully covered if complementary experimental techniques are appropriately combined.

Such coverage of the temporal dimension is comparable to the analysis of the age of the universe in time with µs resolution.

Such “complete” studies of the life cycle of biological samples might be of high interest to obtain all accessible information from biological specimens as it is well known that stimuli activate processes that might lead to effects that are strongly delayed up to variations in the evolutionary development.

Fluorescence spectroscopy provides an extremely valuable tool for long term studies with ps resolution even with pulses which are 100 ps in full width of half maximum. The resolution increases with the squareroot of the energy used for the measurement. The principal limitations allow a much better resolution than widely assumed, but the complexity and frequently the vital dynamics of the sample makes it impossible to investigate all structures and their dynamics in detail.

Further studies employing complementary experimental techniques covering the whole hierarchic organization in space and time are therefore recommended for deep and detailed analysis.

6. Acknowledgements

Financial support by BMBF RUS 10/026, 11/014 and BMBF project "Quantum" (FKZ 13N10076) is gratefully acknowledged. V.Z. Paschenko and E.G. Maksimov also thank the Russian Foundation for Basic Research (project no. 11-04-01617 and no. 12-04-31100). This work was also supported by grants from the Russian Foundation for Basic Research (nos. 11-04-01389a, 12-04-92101, 13-04-91372, 13-04-92711), by Molecular and Cell Biology Programs of the Russian Academy of Sciences, by BMBF (No: 8125) Bilateral Cooperation between Germany and Russia, to S.I.A. T. Friedrich and F.-J. Schmitt acknowledge COST for financial support in the framework of COST action MP1205. The Authors acknowledge Marco Vitali for his steady Support on the Flim measurements and Florian Schmitt for drawing the Figures 1 and 2.

References

1. Adolphs J., Renger T. (2006), How Proteins Trigger Excitation Energy Transfer in the FMO Complex of Green Sulfur Bacteria. Biophysical Journal, 91(8): 2778–2797.
2. Agarwal R., Krueger B.P., Scholes G.D., Yang M., Yom J., Mets L., Fleming G.R. (2000), Ultrafast Energy Transfer in LHC-II Revealed by Three-Pulse Photon Echo Peak Shift Measurements. J Phys Chem B, 104(13): 2908–2918.
3. Allakhverdiev S.I., Tomo T., Shimada Y., Kindo H., Nagao R., Klimov V.V., Mimuro M. (2010), Redox potential of pheophytin a in photosystem II of two cyanobacteria having the different special pair chlorophylls. Proc Natl Acad Sci USA, 107(8): 3924-3929.
4. Allakhverdiev S.I., Tsuchiya T., Watabe K., Kojima A., Los D.A., Tomo T., Klimov V.V., Mimuro M. (2011), Redox potentials of primary electron acceptor quinone molecule (QA)- and conserved energetics of photosystem II in cyanobacteria with chlorophyll a and chlorophyll d. Proc Natl Acad Sci U S A, 108(19): 8054-8058.
5. Andresen M., Stiel A.C., Trowitzsch S., Weber G., Eggeling C., Wahl M.C., Hell S.W., Jakobs S. (2007), Structural basis for reversible photoswitching in Dronpa. Proc Natl Acad Sci USA, 104(32): 13005–13009.
6. Andresen M., Wahl M.C., Stiel A.C., Gräter F., Schäfer L.V., Trowitzsch S., Weber G., Eggeling C., Grubmüller H., Hell S.W., Jakobs S. (2005), Structure and mechanism of the reversible photoswitch of a fluorescent protein. Proc Natl Acad Sci USA, 102(37): 13070–13074.
7. Annamalai P., Yanagihara S. (1999), Identification and characterization of a heat-stress induced gene in cabbage encodes a Kunitz type protease inhibitor. J Plant Physiol, 155(2): 226–233.
8. Barinov A.V., Goryachev N.S., Schmitt F.-J., Renger G., Kotel'nikov A.I. (2009), Luminescent Analysis of Microsecond Relaxation Dynamics of Viscous Media, Optics and Spectroscopy (Condensed matter spectroscopy), 107(1), 95–100
9. Bawendi M.G., Carroll P.J., Wilson W.L., Brus L.E. (1992), Luminescence properties of CdSe quantum crystallites: Resonance between interior and surface localized states. J Chem Phys, 96(2): 946–954.
10. Becker & Hickl GmbH (2006a), PML-16-C 16 Channel Detector Head for Time-Correlated Single Photon Counting User Handbook. Berlin, http://www.becker-hickl.de/pdf/pml16c21.pdf
11. Becker & Hickl GmbH (2006b), The bh TCSPC Handbook. Berlin, http://www.becker-hickl.de/handbook.htm
12. Belyaeva N.E., Schmitt F.-J., Paschenko V.Z., Riznichenko G.Y., Rubin A.B., Renger G. (2011), PS II model based analysis of transient fluorescence yield measured on whole leaves of Arabidopsis thaliana after excitation with light flashes of different energies. BioSystems, 103(2): 188–195.
13. Belyaeva N.E., Schmitt F.-J., Steffen R., Paschenko V.Z., Riznichenko G.Yu., Chemeris Yu.K., Renger G., Rubin A.B. (2008), PS II model-based simulations of single turnover flash-induced transients of fluorescence yield monitored within the time domain of 100 ns–10 s on dark-adapted Chlorella pyrenoidosa cells. Photosynth Res, 98(1–3): 105–119.
14. Brakemann T., Stiel A., Weber G., Andresen M., Testa I., Grotjohann T., Leutenegger M., Plessmann U., Urlaub H., Eggeling C., Wahl M.C., Hell S.W., Jakobs S. (2011), A reversibly photoswitchable GFP-like protein with fluorescence excitation decoupled from switching. Nat Biotechnol, 29: 942–947.
15. Debreczeny M.P., Sauer K., Zhou J., Bryant D.A. (1995a), Comparison of Calculated and Experimentally Resolved Rate Constants for Excitation Energy Transfer in C-Phycocyanin. 1. Monomers. J Phys Chem, 99(20): 8412–8419.
16. Debreczeny M.P., Sauer K., Zhou J., Bryant D.A.

(1995b), Comparison of Calculated and Experimentally Resolved Rate Constants for Excitation Energy Transfer in C-Phycocyanin. 2. Trimers. J Phys Chem, 99(20): 8420–8431.

17. Dedecker P., Hotta J., Flors C., Sliwa M., Uji-i H., Roeffaers M., Ando R., Mizuno H., Miyawaki A., Hofkens J. (2007), Subdiffraction imaging through the selective donut-mode depletion of thermally stable photoswitchable fluorophores: numerical analysis and application to the fluorescent protein Dronpa. J Am Chem Soc, 129(51): 16132–16141.
18. Dempski R.E., Friedrich T., Bamberg E. (2009), Voltage clamp fluorometry: Combining fluorescence and electrophysiological methods to examine the structure-function of the Na+/K+-ATPase. BBA Bioenergetics, 1787(6): 714–720.
19. Downing W.L., Mauxion F., Fauvarque M.O., Reviron M.P., de Vienne D., Vartanian N., Giraudat J. (1992), A Brassica napus transcript encoding a protein related to the Künitz protease inhibitor family accumulates upon water stress in leaves, not in seeds. Plant J, 2(5): 685–693.
20. Eggeling C., Hilbert M., Bock H., Ringemann C., Hofmann M., Stiel A., Andresen M., Jakobs S., Egner A., Schönle A., Hell S.W. (2007), Reversible photoswitching enables single-molecule fluorescence fluctuation spectroscopy at high molecular concentration. Microsc Res Tech, 70(12): 1003–1009.
21. Eggeling C., Widengren J., Rigler R., Seidel C. (1998), Photobleaching of Fluorescent Dyes under Conditions Used for Single-Molecule Detection: Evidence of Two-Step Photolysis. Anal Chem, 70(13): 2651–2659.
22. Freer A., Prince S., Sauer K., Papiz M., Lawless A.H., McDermott G., Cogdell R., Isaacs N.W. (1996), Pigment–pigment interactions and energy transfer in the antenna complex of the photosynthetic bacterium Rhodopseudomonas acidophila. Structure, 4(4): 449–462.
23. Geibel S., Kaplan J.H., Bamberg E., Friedrich T. (2003), Conformational dynamics of the Na+/K+-ATPase probed by voltage clamp fluorometry. Proc Natl Acad Sci USA, 100(3): 964–969.
24. Gillbro T., Sandström A., Sundström V., Wendler J., Holzwarth A.R. (1985), Picosecond Study of energy transfer kinetics in phycobilisomes of *Synechococcus* 6301 and the Mutant AN 112. Biochimica et Biophysica Acta, 808(1): 52–65.
25. Glazer A.N. (1985), Light harvesting by phycobilisomes. Ann Rev Biophys Chem, 14: 47–77.
26. Gordon G.W., Berry G., Liang X.H., Levine B., Herman B. (1998), Quantitative Fluorescence Resonance Energy Transfer Measurements Using Fluorescence Microscopy. Biophysical Journal. 74(5): 2702–2713.
27. Green B., Parson W.W. eds. (2003), Light Harvesting Antennas. Advances in Photosynthesis and Respiration. Springer, Dordrecht, Vol. 13.
28. Gross L., Mohn F., Moll N., Liljeroth P., Meyer G. (2009), The Chemical Structure of a Molecule Resolved by Atomic Force Microscopy. Science, 325(5944): 1110–1114.
29. Häder D.-P. (1999), Photosynthese. Thieme Verlag Stuttgart.
30. Heath O.V.S. (1972), Physiologie der Photosynthese. Thieme Verlag Stuttgart.
31. Hell S.W. (2004), Strategy for far-field optical imaging and writing without diffraction limit. Phys Lett A, 326: 140–145.
32. Hofmann M., Eggeling C., Jakobs S., Hell S.W. (2005), Breaking the diffraction barrier in fluorescence microscopy at low light intensities by using reversibly photoswitchable proteins. Proc Natl Acad Sci USA, 102(49): 17565–17569.
33. Holtzwarth A.R. (1991), Structure-function relationships and energy transfer in phycobiliprotein antennae. Physiologia plantarum, 83(3): 518–528.
34. Holzwarth A.R., Suter G.W. (1987), A kinetic model for the energy transfer in phycobilisomes. Biophys, 52(5): 673–683.
35. Horigome D., Satoh H., Itoh N., Mitsunaga K., Oonishi I., Nakagawa A., Uchida A. (2007), Structural mechanism and photoprotective function of water-soluble chlorophyll-binding protein. J Biol Chem, 282(9): 6525–6531.
36. Hu Q., Marquardt J., Iwasaki I., Miyashita H., Kurano N., Mörschel E., Miyachi S. (1999), Molecular structure, localization and function of phycobiliproteins in the chlorophyll *a/d* containing oxygenic photosynthetic prokaryote *Acaryochloris marina*. Biochim. Biophys. Acta, 1412(3): 250–261.
37. Hu Q., Miyashita H., Iwasaki I., Kurano N., Miyachi S., Iwaki M., Itoh S. (1998), A photosystem I reaction center driven by chlorophyll *d* in oxygenic photosynthesis. Proc Natl Acad Sci USA, 95(22): 13319–13323.
38. Hughes J.L., Razeghifard R., Logue M., Oakley A., Wydrzynski T., Krausz E. (2006), Magneto-Optic Spectroscopy of a Protein Tetramer Binding Two Exciton-Coupled Chlorophylls. J Am Chem Soc, 128(11): 3649–3658.
39. Ke B. (2001), Photosynthesis. Kluwer Academic: Dordrecht, The Netherlands, Vol. 10.
40. Ketelaars M., van Oijen A.M., Matsushita M., Köhler J., Schmidt J., Aartsma T.J. (2001), Spectroscopy on the B850 Band of Individual Light-Harvesting 2 Complexes of Rhodopseudomonas acidophila I. Experiments and Monte Carlo simulations. Biophysical Journal, 80(3): 1591–1603.
41. Kim D., So P.T.C. (2006), Photon counting by large-area detection with multianode photomultiplier tube in high-throughput multiphoton microscopy. SPIE Proc., 6372.
42. Klar T.A., Jakobs S., Dyba M., Egner A., Hell S.W. (2000), Fluorescence microscopy with diffraction

resolution limit broken by stimulated emission. Proc Natl Acad Sci USA, 97(15): 8206–8210.
43. Krikunova M., Voigt B., Lokstein H. (2002), Direct evidence for excitonically coupled chlorophylls *a* and *b* in LHC II of higher plants by non-linear polarization spectroscopy in the frequency domain. Biochim Biophys Acta, 1556(1): 1–5.
44. Lakowicz J.R. (2006), Principles of fluorescence spectroscopy. Springer, New York, pp. 954.
45. Lambrev P.H., Schmitt F.-J., Kussin S., Schoengen M., Várkonyi Z., Eichler H.J., Garab G., Renger G. (2011), Functional domain size in isolated aggregates of light-harvesting complex II and thylakoid membranes. Biochim Biophys Acta, 1807(9): 1022–1031.
46. Lawlor D.W., Häder D.-P. (1990), Photosynthese. Thieme Verlag Stuttgart.
47. Lebedev N., Trammell S., Griva I., Spano A. (2006), New bio-inorganic photo-electronic devices based on photosynthetic proteins. Proc. SPIE, 6370.
48. Marquardt J., Senger H., Miyashita H., Miyachi S., Mörschel E. (1997), Isolation and characterization of biliprotein aggregates from *Acaryochloris marina*, a Prochloron-like prokaryote containing mainly chlorophyll *d*. FEBS Lett, 410(2): 428–432.
49. Medintz I.L., Mattoussi H. (2009), Quantum dot-based resonance energy transfer and its growing application in biology. Phys Chem Chem. Phys, 11: 17–45.
50. Mimuro M. (2004), Photon capture, exciton migration and fluorescence emission in cyanobacteria and red algae. In: Chlorophyll a Fluorescence: A Signature of Photosynthesis (Papageorgiou G.C., Govindjee eds.). Springer, Dordrecht, The Netherlands, p. 173–195.
51. Mimuro M., Akimoto S., Gotoh T., Yokono M., Akiyama M., Tsuchiya T., Miyashita H., Kobayashi M., Yamazaki I. (2004), Identification of the primary electron donor in PS II of the Chl *d*-dominated cyanobacterium *Acaryochloris marina*. FEBS Lett, 556(1–3): 95–98.
52. Mimuro M., Akimoto S., Yamazaki I., Miyashita H., Miyachi S. (1999), Fluorescence properties of Chlorophyll *d*-dominating prokaryotic alga, *A. marina* : studies using time-resolved fluorescence spectroscopy on intact cells. Biochim Biohys Acta, 1412(1), 37–46.
53. Miyashita H., Ikemoto H., Kurano N., Adachi K., Chihara M., Miyachi S. (1996), Chlorophyll *d* as a major pigment. Nature (London), 383: 402.
54. Müh F., Madjet Mel-A, Adolphs J., Abdurahman A., Rabenstein B., Ishikita H., Knapp E.-W., Renger T. (2007), Alpha-helices direct excitation energy flow in the Fenna Matthews Olson protein. Proc Natl Acad Sci USA, 104(43): 16862–16867.
55. Mullineaux C.W., Holzwarth A.R. (1991), Kinetics of excitation energy transfer in the cyanobacterial phycobilisome-Photosystem II complex. Biochim Biophys Acta, 1098(1): 68–78.
56. Nishio N., Satoh H. (1997), Water-soluble chlorophyll protein in cauliflower may be identical to BnD22, a drought-induced, 22-kilodalton protein in rapeseed. Plant Physiol, 115(2): 841–846.
57. Park T.S., Schulten K. (2001), Kinetics of excitation migration and trapping in the photosynthetic unit of purple bacteria. Journal of Physical Chemistry B, 105(34): 8259–8267.
58. Petrášek Z., Schmitt F.-J., Theiss Ch., Huyer J., Chen M., Larkum A., Eichler H.J., Kemnitz K., Eckert H.-J. (2005), Excitation energy transfer from Phycobiliprotein to Chlorophyll d in intact cells of Acaryochloris marina studied by time- and wavelength resolved fluorescence spectroscopy. Photochem Photobiol Sci, 4(12): 1016–1022.
59. Pieper J., Irrgang K.-D., Rätsep M., Voigt J., Renger G., Small G. (2000), Assignment of the Lowest QY-state and Spectral Dynamics of the CP29 Chlorophyll *a/b* Antenna Complex of Green Plants: A Hole-burning Study. Photochem Photobiol, 71(5): 574–581.
60. Pieper J., Ratsep M., Trostmann I., Schmitt F.-J., Theiss C., Paulsen H., Eichler H.J., Freiberg A., Renger G. (2011), Excitonic Energy Level Structure and Pigment-Protein Interactions in the Recombinant Water-Soluble Chlorophyll Protein (WSCP), Part II: Spectral Hole-Burning Experiments. J Phys Chem B, 115(14): 4053–4065.
61. Renger G. (2008), In: Primary processes of photosynthesis (Renger G. ed.). RSC Publ., Cambridge, U.K., Vol. I: Basic principles and apparatus.
62. Renger G. (2010), The light reactions of photosynthesis. Curr Sci, 98(10): 1305–1319.
63. Renger G., Pieper J., Theiss C., Trostmann I., Paulsen H., Renger T., Eichler H.J., Schmitt F.-J. (2011), Water soluble chlorophyll binding protein of higher plants: a most suitable model system for basic analyses of pigment-pigment and pigment-protein interactions in chlorophyll protein complexes. J Plant Physiol, 168(12): 1462–1472.
64. Renger T., Kühn O. (2007), Molekulare Energietrichter. Wissenschaftsmagazin fundiert. Energie, 1/2007, FU Berlin ISSN: 1616–524.
65. Renger T., Madjet M.E., Müh F., Trostmann I., Schmitt F.-J., Theiss C., Paulsen H., Eichler H.J., Knorr A., Renger G. (2009), Thermally Activated Superradiance and Intersystem Crossing in the Water-Soluble Chlorophyll Binding Protein. J Phys Chem B, 113(29): 9948–9957.
66. Renger T., Trostmann I., Theiss C., Madjet M.E., Richter M., Paulsen H., Eichler H.J., Knorr A., Renger G. (2007), Refinement of a structural model of a pigment-protein complex by accurate optical line shape theory and experiments. J Phys Chem B, 111(35): 10487–10501.
67. Reviron M., Varantian N., Sallantin M., Huet J., Pernollet J., de Vienne D. (1992), Characterization of a Novel Protein Induced by Progressive or Rapid Drought

and Salinity in Brassica napus Leaves. Plant Physiol, 100(3): 1486–1493.
68. Rigler R., Mets Ü. (1992), Diffusion of Single Molecules through a Gaussian Laser Beam. SPIE proc., 1921: 239–248.
69. Rigler R., Mets Ü., Widengren J., Kask P. (1993), Fluorescence correlation spectroscopy with high count rate and low background: analysis of translational diffusion. European Biophysics Journal, 22(1590): 169–175.
70. Sarkar A., Robertson R.B., Fernandez J.M. (2004), Simultaneous atomic force microscope and fluorescence measurements of protein unfolding using a calibrated evanescent wave. Proc Natl Acad Sci USA, 101(35): 12882–12886.
71. Satoh H., Nakayama K., Okada M.J. (1998), Molecular cloning and functional expression of a water-soluble chlorophyll protein, a putative carrier of chlorophyll molecules in cauliflower. J Biol Chem, 273(46): 30568–30575.
72. Satoh H., Uchida A., Nakayama K., Okada M. (2001), Water soluble Chlorophyll Protein in Brassicaceae Plants is a Stress-Induced Chlorophyll-Binding Protein. Plant Cell Physiol, 42(9): 906–911.
73. Schatz G., Brock H., Holtzwarth A.R. (1988), Kinetic and energetic model for the primary processes in photosystem II. Biophys Journal, 54(3): 397–405.
74. Scheuring S., Reiss-Husson F., Engel A., Rigaud J.-L., Ranck J.-L. (2001), High-resolution AFM topographs of Rubrivivax gelatinosus light-harvesting complex LH2. The EMBO Journal, 20(12): 3029–3035.
75. Schlodder E., Çetin M., Eckert H.-J., Schmitt F.-J., Barber J., Telfer A. (2007), Both Chlorophylls *a* and *d* are essential for the photochemistry in photosystem II of the cyanobacterium, *Acaryochloris marina*. Biochim Biophys Acta, 1767(6): 589–595.
76. Schmidt K., Fufezan C., Krieger-Liszkay A., Satoh H., Paulsen H. (2003), Recombinant water-soluble chlorophyll protein from *Brassica oleracea Var. botrys* binds various chlorophyll derivatives. Biochemistry, 42(24): 7427–7433.
77. Schmitt F.-J. (2008), Resolution limits of time- and space-correlated single photon counting. In: Proceedings of the 2008 international conference on information theory and statistical learning ITSL (Dehmer M., Drmota M., Emmert-Streib F. eds.). ISBN: 1-60132-079-5, p. 91–97.
78. Schmitt F.-J. (2009), The lower bound on the energy for bounded systems is equivalent to the Bekenstein upper bound on the entropy to energy ratio for bounded systems. arXiv:0901.3686v1 [hep-th].
79. Schmitt F.-J. (2010), Temperature induced conformational changes in hybrid complexes formed from CdSe/ZnS nanocrystals and the phycobiliprotein antenna of Acaryochloris marina. Journal of Optics, 12(8). doi:10.1088/2040-8986/12/8/084008.
80. Schmitt F.-J. (2011), Picobiophotonics fort he investigation of pigment-pigment and pigment-protein interaction in photosynthetic complexes. PhD Thesis. TU Berlin.
81. Schmitt F.-J., Fuesers J., Südmeyer H., Börner J., Jeyasangar V., Olliges R., Maksimov E.G., Grehn M., Theiss C., Paschenko V.Z., Eichler H.J., Renger G. (2010), Simulations of energy transfer processes along the rod shaped PBP antenna and Chl *d* antenna of *A.marina*. In: AIP conference proceedings (Vainos N.A., Pissadakis S., Couris S., Paspalakis E., Koutselas I. eds.), 1288, ISBN 978-0-7354-0843-2, ISSN: 0094234X.
82. Schmitt F.-J., Maksimov E.G., Hätti P., Weißenborn J., Jeyasangar V., Razjivin A.P., Paschenko V.Z., Friedrich T., Renger G. (2012), Coupling of different isolated photosynthetic light harvesting complexes and CdSe/ZnS nanocrystals via Förster resonance energy transfer. Biochim Biophys Acta, 1817(8): 1461–1470.
83. Schmitt F.-J., Maksimov E.G., Suedmeyer H., Jeyasangar V., Theiss C., Paschenko V.Z., Eichler H.J., Renger G. (2011), Time resolved temperature switchable excitation energy transfer processes between CdSe/ZnS nanocrystals and phycobiliprotein antenna from Acaryochloris marina. Photon Nanostruct: Fundam Appl, 9(2): 190–195.
84. Schmitt F.-J., Theiss C., Wache K., Fuesers J., Andree S., Handojo A., Karradt A., Kiekebusch D., Eichler H.J., Eckert H.-J. (2006), Investigation of the excited states dynamics in the Chl d- containing cyanobacterium Acaryochloris marina by time- and wavelength correlated single-photon counting. Proc. SPIE, 6386(7).
85. Schmitt F.-J., Trostmann I., Theiss C., Pieper J., Renger T., Fuesers J., Hubrich E.H., Paulsen H., Eichler H.J., Renger G. (2008), Excited State Dynamics in Recombinant Water-Soluble Chlorophyll Proteins (WSCP) from Cauliflower Investigated by Transient Fluorescence Spectroscopy. J Phys Chem B, 112(44): 13951–13961.
86. Schoeps O. (2009), Optical Spectroscopy on SemiconductorNanocrystals: Emission Dynamics on a Nanoscale. PhD Thesis. TU Dortmund.
87. Schrödinger E. (1989), Was ist Leben?: Die lebende Zelle mit den Augen des Physikers betrachtet. Piper München, 10.
88. Schulten K. (1999), From simplicity to complexity and back: Function, architecture and mechanism of light harvesting systems in photosynthetic bacteria. In: Simplicity and Complexity in Proteins and Nucleic Acids (Frauenfelder H., Deisenhofer J., Wolynes P.G. eds.). Dahlem University Press, Berlin, p. 227–253.
89. Selanger K.A., Falnes J., Sikkeland T. (1977), Fluorescence lifetime studies of Rhodamine 6G in methanol. The Journal of Physical Chemistry, 81: 1960–1963.
90. Shaner N.C., Steinbach P.A., Tsien R.Y. (2005), A guide to choosing fluorescent proteins. Nature Methods, 2(12):

905–909.
91. Sharkov A.V., Kryukov I., Khoroshilov E.V., Kryukov P.G., Fischer R., Scheer H., Gillbro T. (1994), Femtosecond spectral and anisotropy study of excitation energy transfer between neighbouring α-80 and β-81 chromophores of allophycocyanin trimers. Biochimica et Biophysica Acta, 1188(3): 349–356.
92. Stepanenko O.V., Shcherbakova D.M., Kuznetsova I.M., Turoverov K.K., Verkhusha V. (2011), Modern fluorescent proteins: from chromophore formation to novel intracellular applications. BioTechniques, 51(5): 313–327.
93. Talaga D.S. (2006), Information Theoretical Approach to Single-Molecule Experimental Design and Interpretation. J Phys Chem A, 110(31): 9743–9757.
94. Theiss C. (2006), Transiente femtosekunden-absorptionsspektroskopie des Anregungs-Energietransfers in isolierten Pigment-Proteinkomplexen des Photosyntehseapparates. PhD Thesis. TU Berlin.
95. Theiss C., Andree S., Schmitt F.-J., Renger T., Trostmann I., Eichler H.J.,Paulsen H., Renger G. (2007), Pigment−Pigment and Pigment−Protein Interactions in Recombinant Water-Soluble Chlorophyll Proteins (WSCP) from Cauliflower. J Phys Chem B, 111(46): 13325–13335.
96. Theiss C., Schmitt F.-J., Andree S., Cardenas-Chavez C., Wache K., Fuesers J., Vitali M., Wess M., Kussin S., Eichler H.J., Eckert H.-J. (2008), Excitation Energy Transfer in the Phycobiliprotein Antenna of Acaryochloris marina Studied by Transient fs Absorption and Fluorescence Spectroscopy. In: Photosynthesis. Energy from the Sun (Allen J.F., Gantt E., Golbeck J.H., Osmond B. eds.). Springer, Dordrecht, The Netherlands, p. 339–342.
97. Theiss C., Schmitt F.-J., Pieper J., Nganou C., Grehn M., Vitali M., Olliges R., Eichler H.J., Eckert H.-J. (2011), Excitation energy transfer in intact cells and in the phycobiliprotein antennae of the chlorophyll d containing cyanobacterium Acaryochloris marina. J Plant Physiol, 168(12): 1473–1487.
98. Tomo T., Allakhverdiev S.I., Mimuro M. (2011), Constitution and energetics of photosystem I and photosystem II in the chlorophyll d-dominated cyanobacterium Acaryochloris marina. J Photochem Photobiol B, 104(1-2): 333-340.
99. Trissl H.-W. (2003), Modeling the Excitation Capture in Thylakoid Membranes. In: Photosynthesis in Algae (Larkum T.W. ed.). Kluwer Academic Publishers, p. 245–276.
100. Tsien R.Y. (2008), The green fluorescent protein. Annu Rev Biochem, 67: 509–544.
101. Vickery S.A., Dunn S.U. (2000), Combining AFM and FRET for high resolution fluorescence microscopy. Journal of Microscopy, 202(2): 408–412.
102. Vitali M. (2011), Long-term observation of living cells by wide-field fluorescence lifetime imaging microscopy. PhD Thesis. TU Berlin.
103. Wen J., Zhang H., Gross M.L., Blankenship R. (2011), Native electrospray mass spectrometry reveals the nature and stoichiometry of pigments in the FMO photosynthetic antenna protein. Biochemistry, 50(17): 3502–3511.
104. Westphal J.V., Hell S.W. (2005), Nanoscale resolution in the focal plane of an optical microscope. Phys Rev Lett, 94(14): 143903–143906.
105. Westphal V., Seeger J., Salditt T., Hell S.W. (2005), Stimulated emission depletion microscopy on lithographic nanostructures. J Phys B: At. Mol. Opt. Phys., 38(9): 695–705.
106. Yano J., Kern J., Sauer K., Latimer M.J., Pushkar Y., Biesiadka J., Loll B., Saenger W., Messinger J., Zouni A., Yachandra V.K. (2006), Where water is oxidized to dioxygen: structure of the photosynthetic Mn4Ca cluster. Science, 314(5800): 821–825.
107. Yoon I., Li J.Z., Shim Y.K. (2013), Advance in Photosensitizers and Light Delivery for Photodynamic Therapy. Clin Endosc, 46(1): 7–23.